

Photometry and the Metallicity Distribution of the Outer Halo of M31

Patrick R. Durrell¹

*Department of Physics & Astronomy, 2219 Main Mall, University of British Columbia,
Vancouver, BC V6T 1Z4 CANADA*

and

*Department of Astronomy & Astrophysics, The Pennsylvania State University, 525 Davey Lab,
University Park, PA 16802 USA²*

`pdurrell@astro.psu.ca`

William E. Harris¹

Department of Physics & Astronomy, McMaster University, Hamilton, ON L8S 4M1 CANADA

`harris@physics.mcmaster.ca`

and

Christopher J. Pritchett

Department of Physics & Astronomy, University of Victoria, Victoria, BC V8W 3P6 CANADA

`pritchet@clam.phys.uvic.ca`

ABSTRACT

We have conducted a wide-field CCD-mosaic study of the resolved red-giant branch stars of M31, in a field located 20 kpc from the nucleus along the SE minor axis. In our $(I, V - I)$ color-magnitude diagram, red-giant branch (RGB) stars in the top three magnitudes of the M31 halo are strongly present. We use photometry of a more distant control field to subtract field contamination and then to derive the “cleaned” luminosity function and metallicity distribution for this outer-halo region of M31. From the color distribution of the foreground Milky Way halo stars, we find a reddening $E(V - I) = 0.10 \pm 0.02$ for this field, and from the luminosity of the RGB tip, we determine a distance modulus $(m - M)_o = 24.47 \pm 0.12$ ($= 783 \pm 43$ kpc). The metallicity distribution function (MDF) is derived from interpolation within an extensive new grid

¹Visiting Astronomer, Canada-France-Hawaii Telescope, operated by the National Research Council of Canada, le Centre National de la Recherche Scientifique de France, and the University of Hawaii

²current address

of RGB models (Vandenbergh et al. 2000). We find that the MDF is dominated by a moderately high-metallicity population ($[m/H] \sim -0.5$) that has previously been found in more interior M31 halo/bulge fields, and is very much more metal-rich than the $[m/H] \sim -1.5$ level which characterizes the Milky Way halo. In addition, a significant ($\sim 30\% - 40\%$, depending on AGB star contribution) metal-poor population is also present. To first order, the total shape of the MDF resembles that predicted by a simple, single-component model of chemical evolution starting from primordial gas with an effective yield $y = 0.0055$. It strongly resembles the MDF recently found for the outer halo of the giant elliptical NGC 5128 (Harris et al. 2000), though NGC 5128 has an even lower fraction of low-metallicity stars. Intriguingly, in both NGC 5128 and M31, the metallicity distribution of the *globular clusters* in M31 does not match the halo *stars*, in the sense that the clusters are far more heavily weighted to metal-poor objects. We suggest similarities in the formation and early evolution of massive, spheroidal stellar systems.

Subject headings: galaxies: halos — galaxies: individual (M31) — galaxies : photometry— galaxies: stellar content — Local Group

1. Introduction

While the stellar halo may be but a minor constituent in the total mass and luminosity of a galaxy, it is an important tracer of the conditions of the formation and earliest evolution of galaxies. Studies of the halo stars and globular clusters in our own Milky Way have provided a wealth of insight into the early chemical evolution of the Galaxy, including its use as a chronometer to probe formation timescales and models. Our location within the MW, however, makes the study of more global properties of our halo (such as its radial extent, age distribution, chemical composition – all of which require large, complete datasets) very difficult, since in a given star field there are far more local disk stars than halo stars, usually by over 3 orders of magnitude. Monumental ‘needle in a haystack’ efforts to both find and study MW halo stars have been made (eg. Beers et al. 1996; Carney et al. 1996; Sommer-Larsen et al. 1997, and references within); and further ambitious studies are currently underway (Totten & Irwin 1998; Majewski et al. 2000; Morrison et al. 2000; Ivezić et al. 2000).

A different, yet equally interesting, approach is to study the halo stars in nearby galaxies where the stars are at a common distance, relieving one of the primary difficulties with studying most MW halo populations. The halo of the spiral galaxy M31 provides us with a nearby and readily accessible population of large numbers of halo stars; photometry of its red-giant branch (RGB) stars down to the level of the horizontal branch is easily carried out with 4-meter-class telescopes. M31 is also of earlier Hubble type (Sb vs. SBbc) and more massive than the Milky Way (with a higher proportion in the bulge/spheroid component, eg. Courteau & van den Bergh 1999; Freeman

1999; Côté et al. 2000b, and references within; but see Evans & Wilkinson 2000). Unlike the MW bulge, the larger bulge of M31 follows an $r^{1/4}$ profile (Pritchett & van den Bergh 1994, hereafter PvdB94), and thus it is of interest to understand the bulge and halo in both galaxies to investigate any contrasts in formation mechanisms (see also Wyse, Gilmore & Franx 1997; Morrison 1999). We will find that the M31 halo stars are indeed strikingly different on average from those in the Milky Way.

While spectroscopy of stars in M31 is difficult and time-consuming (see Reitzel & Guhathakurta 2001, for some first results), it is not hard to obtain photometry of the RGB stars through metallicity-sensitive indices to study the metallicity distribution function (MDF) in its broad terms. Mould & Kristian (1986) were the first to clearly resolve the RGB stars, in a field 7 kpc from the galaxy center along the southern minor axis. Their data indicated that the M31 halo there has $[\text{Fe}/\text{H}] \sim -0.6$, more metal-rich by a factor of a few than the MW halo. Mould (1986) performed a similar study on fields located 5, 12 and 20 kpc from M31 along the minor axis; analysis of the 12 kpc field showed a similarly high metallicity, but contamination made results from the other 2 fields less certain. Deeper ground-based studies at other locations in the inner M31 halo ($r_{M31} \sim 7 - 12$ kpc) confirmed the high metallicity for most of the M31 halo population (Pritchett & van den Bergh 1988; Christian & Heasley 1991; Davidge 1993; Durrell, Harris & Pritchett 1994; Couture et al. 1995). Subsequent HST-based CMDs yielded measurements reaching deep enough to show the horizontal-branch stars in its halo clusters and field (Holland, Fahlman & Richer 1996; Rich et al. 1996a,b), and these convincingly showed that a metal-poor component does indeed exist (which had already been suggested by the presence of RR Lyrae stars; Pritchett & van den Bergh 1987). Recent photometric and spectroscopic work by Reitzel, Guhathakurta & Gould (1998) and Reitzel & Guhathakurta (2001) on a field located ~ 20 kpc from M31 indicates that this trend carries into more distant reaches of the halo. Whether or not $[\text{Fe}/\text{H}]$ varies globally with radius is unclear, although van den Bergh & Pritchett (1992) suggested that a strong metallicity gradient does *not* exist in the inner halo based on the $(B - V)$ colors of the RGB.

PvdB94 used star-counts to study the surface brightness profile of the M31 halo for $r < 20$ kpc. Using images with sub-arcsecond seeing to discriminate against most of the faint background galaxies that are the primary source of field contamination, they were able to reach an equivalent surface brightness of $\mu_V \sim 29$, a factor of 10 fainter than reached by conventional surface photometry. They concluded that the entire halo profile along the SE minor axis of M31 was well fit by a single $r^{1/4}$ law profile, falling off steeply at the outer reaches of their survey. However, the PvdB94 CCD fields were quite small by today’s standards ($2' \times 3'$), severely limiting the statistical weight of the data.

In the present paper, we further the star count technique of PvdB94 to study the outer M31 halo, employing significantly larger fields with contemporary CCD mosaic cameras to detect the sparsely spread stars expected in the outer halo. Our primary goals are to derive the stellar density profile, the extent, and the chemical composition of the outer M31 halo, as well as search for substructure that may be the result of smaller dwarf galaxies accreted by M31, since the presence

of such streams has been claimed for the MW halo (eg. Helmi et al. 1999; Ibata et al. 2000; Yanny et al. 2000). We present here the first results from our study, that of a field located ~ 20 kpc from the M31 center along the SE minor axis. The material for other and more remote fields will be discussed in future papers.

2. Observations + Data Reduction

Our first set of observations is a field at $\alpha_{2000} = 0^h48^m30^s$, $\delta_{2000} = +40^\circ17'54''$ (labeled $\mathcal{M}2$ in the nomenclature of PvdB94) located 1.5 SE of the M31 nucleus and roughly along the minor axis. We used the UH8K camera at the Canada-France-Hawaii Telescope (CFHT) on the nights of Sept. 19–23, 1996; three of the four nights were photometric. Exposure times were 4×900 s in V and 3×900 s in I , and the seeing on most images was 0.6 to 0.7 FWHM. The location of the $\mathcal{M}2$ field is plotted in Figure 1, which also illustrates the positions of fields from PvdB94.

Images with similar exposure times as the $\mathcal{M}2$ field were also taken of a background field at $\alpha_{2000} = 1^h20^m35.5^s$, $\delta_{2000} = +41^\circ15'43''$ located 7.1 E of M31. This field (called $\mathcal{R}1$) was chosen to be far enough away from M31 to be free of M31 stars, yet still close enough to provide an adequate control dataset (note that this field is *not* the same as the ‘R1’ field of PvdB94). The seeing for the $\mathcal{R}1$ field was the same as for the $\mathcal{M}2$ field, allowing galaxy/field star discrimination to be similar for both fields. The Galactic latitudes of both fields are $b = -23^\circ$ for $\mathcal{M}2$ and $b = -21^\circ$ for $\mathcal{R}1$, so we expect only small differences in foreground stellar contamination and reddening. Images of 3 other fields (fields $\mathcal{M}3$, $\mathcal{M}4$, and $\mathcal{E}2$ from PvdB94) are located further from M31 and will be discussed in later papers.

The UH8K camera is an 8-CCD mosaic camera (each CCD with 2048×4096 pixels), with a total imaging area of 8192^2 pixels, or a total area of 28.1×28.1 (scale = 0.206 per pixel). One of the chips (chip 4) showed considerable bleeding and other inherent substructure, and was not used in any further analysis. The low QE of another chip (chip 6) was also problematic for the faint photometry crucial to this project, and was thus also not used. The results in this paper are therefore based on 3/4 of the raw UH8K array, covering a rectangular area of $21' \times 28'$ on the sky.

2.1. Data Pre-processing

The program images were pre-processed with bias frames, dark frames and flat-fields, combined in the normal manner through IRAF³.

The primary goal in developing flat-field images for this study was to flatten *each individual*

³IRAF is distributed by the National Optical Astronomy Observatories, which are operated by the Association of Universities for Research in Astronomy, Inc., under cooperative agreement with the National Science Foundation.

chip as much as possible, rather than the entire array at once. We extensively tested different flat-field strategies (described below) in order to derive the best flats. I and V twilight flats were obtained, but were binned 2×2 in order to compensate for the large (7 min) read-out time for the entire array. All flats were then medianed together, resulting in a ‘master’ twilight flat for each chip in each filter. Pre-processing with these flats alone yielded science images flat to $\sim 1\%$.

Dark-sky flats, or ‘super-flats’ (often used for superior flat-fielding in large-field CCDs) were also developed from our (dithered) M31 program fields (20 in V , 15 in I for our total sample). These superflats yielded globally flatter images (typically $\sim 0.3\%$ in I , $\sim 0.5\%$ in V) than the twilight flats, but using the superflats had the small disadvantage of leaving small ‘pits’ on the images which were artifacts from the numerous bright, saturated stars on each image. Numerous algorithms to completely remove these pits had limited success. However, the pits yielded at most $\sim 1\%$ local deviations from the mean sky level, and would have no significant effect on the photometry presented here.

The program images were flat-fielded with either the superflats mentioned above or a ‘master’ flat (where the twilight flats were divided by a heavily smoothed superflat), whichever yielded the flatter image (typically $\sim 0.5\%$ peak-to-peak for each chip).

2.2. Calibration

The photometry was calibrated through Landolt (1992) standards observed on the photometric nights of the observing run. The standards were placed within chip 1 of the mosaic. We created equations for each chip n using average extinction co-efficients from Landolt (1992), employing the method of Harris, Fitzgerald & Reed (1981) :

$$V = v_n - 0.152X + b(V - I) + z(V_1) + \Delta V_{1,n} \quad (1)$$

$$I = i_n - 0.061X + c(V - I) + z(I_1) + \Delta I_{1,n} \quad (2)$$

where X is the mean airmass, $z(V_1)$ and $z(I_1)$ are the zeropoint values derived for chip 1 of the array, and v_n and i_n are the instrumental aperture magnitudes (aperture radius of $3.3''$, and normalized to an exposure time of 1 second) on a given chip n .

As each chip of the mosaic has slightly different QE values, we assumed the colour terms (b , c) of all chips were the same as that for chip 1, and simply made corrections ($\Delta V_{1,n}$, $\Delta I_{1,n}$) in the zeropoint z for each chip in each filter. These zeropoint differences relative to chip 1 were derived from the observed ratios in the sky level. As we had numerous images in each filter to work with, these zeropoint corrections were well determined, with less than 0.01 mag scatter in all cases. There were also no night-night variations in these terms. As a test of our calibration procedure, we reduced images of the globular cluster M92 taken during the same observing run, and found no significant color or magnitude shifts (chip-to-chip) after applying the derived corrections. For all

photometric nights, the color term c in the I equation was consistent with zero, and thus ignored. The color term b in the V equation was $b = -0.034$. The rms scatter of the standard stars in each of the calibration equations was $0.018 - 0.027$ magnitudes.

2.3. Photometry + Image Classification

For each of the fields $\mathcal{M}2$ and $\mathcal{R}1$, the individual CCD images were re-registered, scaled and combined, to construct a single combined image for each filter/chip/field. Each image was weighted before combination so as to maximize the S/N of the final image :

$$w_i \propto \frac{I}{z \sigma^2} \quad (3)$$

where I is the integrated intensity of a star on image i , z is the median sky value, and σ is the stellar FWHM. This function assigns additional weight on images with darker sky levels and smaller stellar images.

Photometry of the objects on each combined image was performed with the stand-alone versions of the DAOPHOT II / ALLSTAR packages (Stetson 1987; Stetson, Davis & Crabtree 1990; Stetson 1992). A single pass of DAOPHOT II + ALLSTAR with a 3.5σ detection threshold was used; since stellar crowding is not significant, a second pass of DAOPHOT did not add significantly to the number of objects detected. A stellar point-spread-function (PSF) was derived from 5-15 bright, uncrowded stars per image. A constant PSF was found to adequately fit the data on all images.

For this project, we are only interested in objects on the images with stellar appearance, so any resolved background galaxies that were not already rejected by DAOPHOT II were subsequently removed with a combination of image parameters: the DAOPHOT χ parameter (Stetson 1987), the r_{-2} and the Δm image moments (Kron 1980). The first two are particularly effective image discriminators (eg. Stetson 1987; Harris et al. 1991; McLaughlin et al. 1995). The appropriate image classification criteria (ie. values which separated the clearly non-stellar objects from stellar ones) were derived for each chip for each filter, and all objects exceeding any *one* of these criteria were considered to be non-stellar and rejected from further analysis. These same criteria were used in the artificial-star experiments that followed (see below), which we used to confirm that very few stellar objects were rejected by any of the adopted criteria.

3. Color-Magnitude Diagrams

The separate V, I results from ALLSTAR and the image classification algorithms were merged (with a matching radius of 1 pixel) to create $I, (V - I)$ color-magnitude diagrams for each field. That of the $\mathcal{M}2$ field is illustrated in Figure 2, and the background $\mathcal{R}1$ field in Figure 3. The total

usable area from the $\mathcal{M}2$ field is 563.6 arcmin², while that of $\mathcal{R}1$ is 548.5 arcmin² (or 0.9732× that of $\mathcal{M}2$); some area in each chip was lost due to the combination of dithered images, as we used only those parts that contained data visible in all separate images to maximize S/N. Both Figures also include error bars that represent typical errors in I and $(V - I)$ for stars with $(V - I) = 1.0$, as determined through artificial star experiments (see next section). The CMDs in Figs. 2 and 3 do not include any objects classified as nonstellar (see previous section). While stars from all six CCDs have been plotted together, the CMDs from the individual chips have slightly different photometric completeness limits (see next section) due to slight QE differences.

The $\mathcal{M}2$ CMD (8691 stars) contains almost twice as many stars as the $\mathcal{R}1$ field (4648 stars), indicating the clear presence of the M31 halo at this distance. Observations of this field by PvdB94 with their far smaller field size yielded only a statistically marginal excess of M31 halo stars. But as also found by Reitzel, Guhathakurta & Gould (1998), the background contamination in this field is large, making the explicit use of a background field extremely helpful to extract the intrinsic properties of the M31 halo population. As is apparent from Figs. 2 and 3, both the halo and background CMDs show a large number of foreground Galactic dwarfs with $17 < I < 20.5$. The total numbers of these stars are quite similar in both CMDs, confirming that we can use $\mathcal{R}1$ directly for field subtraction.

3.1. Artificial Star Experiments

A prime difficulty in using CCD mosaic data is accounting for the slight QE differences between the chips, particularly when treating the combined dataset as a whole. To ascertain both photometric uncertainties and photometric incompleteness in our data, we used the traditional method of adding stars of known brightness to the science frames and re-reducing them. As we are interested in using CMD location (magnitude and color) to isolate likely M31 halo stars, tests were carried out to get statistics on stars in different parts of the $(I, V - I)$ CMD as well.

For each chip of the mosaic, we added a total of 40000 stars (10 runs of 4000 total stars added per run) to the *star-subtracted* science images, and reduced the frames in precisely the same way as described above – a single pass of DAOPHOT II/ALLSTAR, merging of the resulting V and I datasets, and removal of non-stellar images using the image-classification algorithm. The number of artificial stars recovered is similar to that found on the original images, showing that we have adequately re-created the crowding conditions of the original images.

In order to quantify the photometric completeness and uncertainties over the part of the CMD of interest, we added stars in a 2D grid over the range $20.5 < I < 24.0$, $0.0 < (V - I) < 3.0$. The magnitudes were chosen from a steeply rising luminosity function to mimic the LF of the stars in the original science frames. This is illustrated in Figure 4, where the results of all *recovered* artificial stars from chip 1 (as an example) are plotted, and shows not only the photometric incompleteness towards the lower right part of the CMD, but also the increase in photometric uncertainty. From

these experiments it is clear that V incompleteness is the limiting factor in our data.

The limiting magnitudes (m_{lim} ; defined as the 50% completeness level) were derived from all of the artificial star data for each individual chip, and fitting to the following interpolation function (see Fleming et al. 1995) :

$$f(m) = \frac{1}{2} \left(1 - \frac{\alpha(m - m_{lim})}{\sqrt{1 + \alpha^2(m - m_{lim})^2}} \right) \quad (4)$$

where m is either V or I , and α is a parameter that measures how steeply $f(m)$ declines from 1.0 to 0.0; for our data α is typically 3.0 – 4.0, the rather steep transition expected in uncrowded fields. The values for I_{lim} and V_{lim} for each chip are listed in Table 1.

Because the photometric incompleteness varies as a function of I and $(V - I)$ (and on the chip i), we have mapped out the function $f(I, V - I)_i$ using linear interpolation between the grid points sampled in our experiments. We have used this to assign each star in Figures 2 and 3 a completeness fraction f based on $f(I, V - I)_i$ for the chip the star was measured on. While the presented CMDs do not represent photometrically homogeneous datasets, this is accounted for by the assigned f values.

3.2. Reddening

The reddenings $E(V - I)$ of our fields are expected to be similar to that of M31 itself, since it is at high enough Galactic latitude that the reddening should not change steeply with location. The local HI column densities from Burstein & Heiles (1984) yield $E(V - I) = 0.10$ (where we adopt $E(V - I) = 1.25E(B - V)$; Cardelli, Clayton & Mathis 1989; Barmby et al. 2000).

To fine-tune the foreground reddenings a bit further, we have used our CMDs to derive the specific values for each of our program fields, knowing that most of the blue ($V - I \sim 0.6$) stars brighter than $I = 20.5$ on our CMDs are foreground Milky Way halo stars. It is clear from Figures 2 and 3 that there is a relatively sharp blue ‘edge’ to the distribution of these stars, and we interpret this edge as representing the bluest (ie. most metal-poor) turnoff stars in the MW halo. Only a very small fraction of these stars may be blue HB stars in our halo, as there are significantly more turnoff stars in an old stellar population. Using the oft-observed $[Fe/H] \sim -2.2$ globular cluster M92 as a template for such metal-poor stars, we derive a turnoff colour $(V - I)_o = 0.534 \pm 0.015$ based on the fiducial sequence of Johnson & Bolte (1998), and its well determined reddening of $E(V - I) = 0.025 \pm 0.010$ where we have assigned a further uncertainty of ± 0.01 to the Johnson & Bolte turnoff color. This value is consistent with that derived from the turnoff of the similarly metal-poor cluster M30 (Sandquist et al. 1999), although the reddening for M30 is less certain.

In our M31 fields, stars brighter than $I = 21$ and redder than $(V - I) = 0.4$ were used to define color histograms for both fields, as shown in Figure 5. To make an unbiased estimate of

the “edge” color, we first constructed a smoothed histogram from the raw data by treating each star as a unit Gaussian with width $\sigma(V - I)$ and summing all the Gaussians. An edge detection algorithm (basically, a numerical second derivative of the smoothed histogram) was then used to estimate the color at which the numbers of field stars begin to rise most steeply. For the $\mathcal{M}2$ field, we find $(V - I)_e = 0.635$, and for the background field $\mathcal{R}1$, we find $(V - I)_e = 0.615$. Smoothing kernels in the range $\sigma(V - I) = 0.003$ to 0.02 were tried but changed the results only at the ± 0.005 mag level. We adopt ± 0.01 mag for the internal uncertainties in each edge color.

From this analysis we obtain $E(V - I) = 0.10 \pm 0.02$ for the $\mathcal{M}2$ field and $E(V - I) = 0.08 \pm 0.02$ for the $\mathcal{R}1$ field, and we adopt these values for the following discussion. Note that the uncertainties in the absolute reddenings are ± 0.02 , but only ± 0.01 for the reddening *difference* between the two. Both are consistent with the reddening estimates of Burstein & Heiles (1984) and Schlegel, Finkbeiner & Davis (1998) for these locations.

3.3. TRGB Distance to M31

The I -band luminosity function of the $\mathcal{M}2$ field can be used to identify the magnitude level of the tip of the RGB (TRGB), and thus the distance modulus of M31. Before doing this, it is advantageous to use the $\mathcal{R}1$ field to subtract the background luminosity function from $\mathcal{M}2$. For the background field, we first added $\Delta I = 0.03$ and $\Delta(V - I) = 0.02$ to all the stars to account for the slight reddening difference between $\mathcal{R}1$ and $\mathcal{M}2$ (see above). Then, to optimize the count statistics, we first removed from both CMDs the bright stars ($I < 20.5$) bluer than $(V - I) = 1.4$ or redder than $(V - I) = 3.0$, as well as a few fainter stars well to the blue of the RGB population. Next, we constructed a completeness-corrected LF for each field by representing each star with a Gaussian of width $\sigma(I)$ and area $1/f$ where f is the completeness factor at that magnitude and color (see above), then summing all the individual Gaussians. Finally, the residual luminosity function of the M31 giant branch was defined as $LF(I) = LF(\mathcal{M}2) - 1.0275 LF(\mathcal{R}1)$ (where the factor 1.0275 is the total area of $\mathcal{M}2$ relative to $\mathcal{R}1$).

Figure 6 shows the resulting LF, now fully corrected for background and incompleteness. The particular case shown is for a smoothing kernel $\sigma(I) = 0.02$, though we tried values from 0.01 to 0.05 with no noticeable differences. Clearly, for $I < 20$, the $(\mathcal{M}2 - \mathcal{R}1)$ subtraction cancels everything out with only small statistical fluctuations, exactly as it should if there is no significant population of younger, more luminous stars sitting above the old-halo RGB tip. Fainter than this, we see the exponential rise of the RGB itself continuing well past the faint limit of our data.

To estimate the TRGB, we employed the same edge-detection algorithm described earlier to construct a numerical second derivative (slope change) from the smoothed LF. For all trials with different smoothing kernels, a consistent “edge” or sharp increase in the slope of the LF shows up at $I = 20.52 \pm 0.05$. Previous estimates for I_{TRGB} for M31 halo field stars include $I = 20.55 \pm 0.15$ from Mould & Kristian (1986) and $I \sim 20.65$ from Couture et al. (1995). The M31 halo LF of

Holland, Fahlman & Richer (1996) also shows a marked increase in star counts at $I \simeq 20.6$. Our value (which is based on a substantially larger sample of TRGB stars than in previous studies) is in excellent agreement with these values.

To determine the distance to M31, we adopt $M_{I,TRGB} = -4.1 \pm 0.1$ for metal-poor TRGB stars, based on Milky Way globular cluster RGBs and Hipparcos-based globular cluster distances (see Harris et al. 1998; Harris, Harris & Poole 1999). The quoted (random) error simply represents the observed spread in the RGB tip magnitude, and does not include possible systematic errors on the GC distances (which are likely at the ± 0.1 mag level). Our adopted value for $M_{I,TRGB}$ is in excellent agreement with that derived by Ferrarese et al. (2000) from HST-based Cepheid observations to calibrate the TRGB (and other Population II distance indicators). We note that effects of halo depth along the line-of-sight are likely to be small (< 0.05 mag), as the steep radial gradient of the halo (PvdB94) suggests there are relatively few halo stars with $r_{M31} > 20$ kpc, and it is these outermost halo stars that would be far enough in front of M31 to create a systematic bias in the determination of the RGB tip (i.e., there is no strong presence of TRGB stars from the *near* side of the halo).

Using our adopted $M_{I,TRGB}$ gives $(m - M)_I = 24.62 \pm 0.11$ to M31, or a true distance modulus $(m - M)_o = 24.47 \pm 0.12$ once corrected for extinction (where $A_I = 1.48E(V - I) = 0.15 \pm 0.03$). This compares extremely well with other recent estimates of the M31 distance, including Holland (1998) ($(m - M)_o = 24.47 \pm 0.07$ from M31 globular clusters), Stanek & Garnavich (1998) ($(m - M)_o = 24.47 \pm 0.04 \pm 0.05$, red-clump stars), and favorably with most earlier measurements ($(m - M)_o \sim 24.3 \pm 0.1$ from a compilation of methods discussed by van den Bergh 1991, and references within).

4. Analysis

4.1. Metallicity Distribution Function

To construct a metallicity distribution function (MDF) for the M31 halo, we first assume that all of the stars in the CMDs are old ($t > 10$ Gyr), so that the location of the RGB stars in the CMD depends almost solely on metallicity. We then use stars in the top two magnitudes of the RGB to map out the metal abundance $[m/H]$ (defined as $[m/H] = \log(Z/Z_\odot)$, where we have used $Z_\odot = 0.0172$ for consistency with Harris & Harris 2000) defined from interpolation within a fiducial grid of RGB model tracks. Our technique of mapping the I , $(V - I)$ CMD to metallicity is similar to that employed in previous work (eg. Durrell, Harris & Pritchett 1994; Holland, Fahlman & Richer 1996; Harris, Harris & Poole 1999). Here, for the fiducial lines we use the finely spaced grid of the evolutionary tracks by Vandenberg et al. (2000), calibrated in $(V - I)$ color by standard globular cluster fiducial sequences (such as those found in Da Costa & Armandroff 1990). Our methodology follows that of Harris & Harris (2000), whose discussion should be referred to for more detail.

In Figures 7 and 8 we have re-plotted the $\mathcal{M}2$ and $\mathcal{R}1$ CMDs, overlaid with the evolutionary tracks for $0.8 M_{\odot}$ stars from Vandenberg et al. (2000). An empirical shift of -0.03 was applied to the $(V - I)$ color of each model in order to match the metallicities of observed RGBs of Milky Way globular clusters across the entire metallicity range; see Figure 10 of Harris & Harris (2000) and the discussion therein. These models span the range $[\text{Fe}/\text{H}] = -2.31$ to -0.40 . To calibrate the slightly more metal-rich stars we have also added a single $[\text{Fe}/\text{H}] = +0.07$, $t = 12$ Gyr isochrone from Bertelli et al. (1994). The Vandenberg et al. (2000) models assume $[\alpha/\text{Fe}] = +0.3$ (a typical value for Milky Way halo stars), so that the conversion $[\text{m}/\text{H}] \sim [\text{Fe}/\text{H}] + 0.3$ holds for most metallicities. We note the Bertelli et al. RGB is an isochrone and not an evolutionary track, but the distinction is very small for stars in the upper RGB of an old population, and will not affect the analysis that follows.

The model grid was then shifted by the M31 distance modulus ($(m - M)_I = 24.62$) and the appropriate reddening as derived above. The method of determining $[\text{m}/\text{H}]$ from interpolation within the $I, (V - I)$ CMD is the same as that described by Harris & Harris (2000): briefly, $M_{bol} = M_I + (V - I)_o - BC_I$ is calculated for each star, where the bolometric correction BC_I is obtained from the model tables. Then in the $(M_{bol}, (V - I)_o)$ plane bi-linear interpolation is performed on the pair of tracks bracketing the star, from which the metal abundance Z (and thus $[\text{m}/\text{H}]$) is derived. This method was applied to each star in the CMD lying in the region bounded by the model RGBs and in the magnitude range $20.6 < I < 22.5$. Stars more than 0.02 mag *bluer* than the most metal-poor track, as well as stars very near the RGB tip where bi-linear interpolation is less certain, were not used in the analysis. The magnitude range was chosen to minimize the effects of photometric spread on the MDF at fainter I magnitudes, and to avoid the large population of blue objects fainter than $I = 22.5$ that are evident in the $\mathcal{R}1$ field (Figure 8). These objects are most likely faint, unresolved background galaxies; the image classification algorithm is not able to clearly distinguish between stars and galaxies at the faintest levels, leaving most of them to populate the bottom ends of both CMDs. Due to its strong presence in the $\mathcal{R}1$ field, this feature is not an M31 stellar population, and thus not related to the AGB bump found in the M31 CMD by Gallart (1998), which would be located at $I \sim 23.1$. Even if the AGB bump is a strong feature in the halo CMD (which is not clear by inspection of the $\mathcal{M}2$ CMD) it would have no effect on our MDF analysis.

The incompleteness-corrected number of stars in each 0.1-dex metallicity bin for each field is listed in Table 2. The resulting ‘cleaned’ MDF ($\text{MDF}(\text{M31 halo}) = \text{MDF}(\mathcal{M}2) - 1.0275 * \text{MDF}(\mathcal{R}1)$) is plotted in Figure 9 and listed in the final two columns of Table 2. The corrected count (N_c) for each bin is the summation of the $f(I, V - I)^{-1}$ values for each star in each bin, while the errors are simply the Poisson errors ($\pm\sqrt{N}$, where N is the number of observed stars) scaled to the completeness-corrected N_c . From Table 2 it is clear that the background contamination in this part of the CMD ($\sim 25\%$: 3758 stars in $\mathcal{M}2$, and 958 in $\mathcal{R}1$) is distinctly smaller than the $\sim 55\%$ background contamination for the entire magnitude range of the data.

As a check on the effects of photometric errors and incompleteness on our MDF (as well as the

validity of the bulk features present in the Figure 9), we have split the MDF into two magnitude bins ($20.6 < I < 21.6$, $21.6 < I < 22.5$), which are shown individually in Figure 10. The uncertainties in the individual $[m/H]$ values due to the $(V - I)$ photometric scatter have also been placed above representative parts of the MDFs. The close similarity of both MDFs over different parts of the CMD suggests our results are not strongly affected by color shifts in the fainter bin, where the photometric errors are larger. This also indicates that the assumption of a constant color term for all chips in the mosaic (see section 2.2) was acceptable, for more luminous RGB stars reach large $(V - I)$ colors, and extremely discrepant color terms would stretch or shrink the MDF compared to that derived using from fainter stars. In addition, the salient features of the MDF (the strong, sharp peak at $[m/H] \sim -0.5$ and the muted, lower- $[m/H]$ tail) show up in both bins, with remarkable consistency.

We believe the metal-rich ‘edge’ to the MDFs in Figures 9 and 10 is *not* due to photometric incompleteness in V , since for the stars with $I \sim 22$ (lower panel in Figure 10) the $[m/H] \sim -0.3$ ($[Fe/H] \sim -0.61$) model lies well above the 50% completeness level, and at this metallicity it is clear that the MDF is already falling off sharply at the upper end. We note also that the deep photometric studies of Holland, Fahlman & Richer (1996) and Rich et al. (1996a) for inner-halo fields (which should, if anything, be more metal-rich than ours) unequivocally show no evidence for a significant population of solar-metallicity stars.

The MDF of our 20 kpc halo field clearly exhibits the moderately high metallicity suggested by previous studies (see Introduction). The median $[m/H]$ for our entire sample is $[m/H] = -0.66$ ($[Fe/H] \sim -0.96$). Reitzel, Guhathakurta & Gould (1998) reached a similar conclusion for the halo MDF at this distance, albeit with a much smaller field and thus a smaller number of halo stars. But there is a significant metal-poor ‘tail’ in the MDF, as expected from the known presence of RR Lyrae stars in the halo (Pritchet & van den Bergh 1988) and by observations of a small but significant blue component of the M31 HB by Holland, Fahlman & Richer (1996) and Rich et al. (1996a).

To characterize the MDF further, we perform the numerical exercise of fitting a pair of Gaussian functions to the full MDF in Figure 9. The resulting peak values, standard deviations σ and proportions in each Gaussian are listed in Table 3 and plotted in Figure 11. We will refer to each peak as ‘metal-rich’ and metal-poor’ below, though we do not assign these two components any particular physical reality (they overlap heavily, and a more physically based model will be discussed below). The errors listed in Table 3 are the internal uncertainties in the fit. Possible external uncertainties include the adopted reddening and/or distance: A typical error in $E(V - I)$ of ± 0.02 magnitudes produces rather small changes in all three fitted parameters: ± 0.012 dex in the mean $[m/H]$, ± 0.005 dex for σ and $\pm 1.6\%$ for the fraction of stars attributed to each peak. Uncertainties in the distance of ± 0.12 mag have a larger effect, producing changes of ± 0.02 dex for the mean $[m/H]$, ± 0.012 dex for σ , and $\pm 6\%$ for the proportions.

It is noteworthy that the metal-poor part of the MDF (in the sense of the two-component

fit summarized above) nominally makes up a full $40 \pm 2\%(\text{rand.}) \pm 8\%(\text{sys.})$ of the total halo population. However, asymptotic giant branch (AGB) stars *bluer* than the RGB may have exerted small biases on this fraction (recall that we find very few AGB stars *brighter* than the RGB tip, and any such luminous ones will have been masked out in our I selection criteria). The AGB fraction (defined here as the number of AGB stars relative to the number of RGB stars at the same absolute magnitude) from the evolutionary models of Girardi et al. (2000) is 22% (see also Harris, Harris & Poole 1999).

How these AGB stars will affect the MDF is complex, since the color difference between AGB stars and RGB stars varies with both M_I and metallicity. For this reason we have chosen to look simply at the extreme cases of AGB contribution: case A, where all AGB stars related to the metal-rich population stay within the metal-rich population (with a similar assumption for the metal-poor population); and case B, where all metal-rich AGB stars are shifted enough to the blue to become part of the metal-poor region of the MDF, while the metal-poor AGB stars are shifted out of the sample altogether. The true answer should lie between these extremes. In case A the proportions in each of the two components will be as derived with the dual-Gaussian fits described above, with no correction: 40% in the metal-poor component, 60% in the metal-rich component. With case B, we find that $0.22 \times 1674 = 368$ AGB stars from the metal-richer group will appear in the metal-poor component, so that the total metal-poor population should be $(0.402 \times (2800) - 368) = 758$ stars, or 31% of the total RGB population. Taking a simple average and spread of these two extremes, we estimate that the metal-poor component comprises $36 \pm 5\%(\text{rand.}) \pm 8\%(\text{sys.})$ of the total M31 halo population at 20 kpc. Our results are comparable with the estimations of Holland, Fahlman & Richer (1996) where the metal-poor component in their HST fields (located at 7 kpc and 11 kpc from M31) is $\sim 25\%$ to 50% of the total halo stellar population.

4.2. Spatial Distribution

Across the half-degree extent of the $\mathcal{M}2$ field, there is a noticeable gradient in stellar density which reflects the steep falloff of the M31 halo along its minor axis. This effect allows us to examine the spatial distribution of the metal-poor and metal-rich components of the M31 halo MDF defined above, and to find out if any clear differences exist between them. A more thorough investigation of the outer surface brightness profile of M31 using star-counts will appear in a forthcoming paper.

For the purposes of investigating the spatial profile, we avoid the intermediate metallicity range where there is sizeable overlap between the two formally defined Gaussian components defined above. Thus, we define those stars with $-0.3 > [m/H] > -0.6$ as the “metal-rich population”, and the “metal-poor population” those with $[m/H] < -1.0$. For each 0.1-degree radial bin in radius from the center of M31 r_{M31} , we construct the number density ($\sigma = N_c/A$, where N_c is the incompleteness-corrected number of stars in each annulus and A is the area of the annulus in square arc-minutes) profiles for each component. The results are plotted in log-log form in Figure 12. This plot shows that stars in both populations of the MDF follow a very steep profile, confirming the

number counts seen by PvdB94. Fitting the data to the function $\sigma \propto r^\gamma$ with least-squares yields $\gamma = -5.25 \pm 0.63$ (fitting uncertainty only) and $\gamma = -6.54 \pm 0.59$ for the metal-poor and metal-rich distributions. However, the χ^2 values are rather large (primarily due to the high metal-rich point at $r_{M31} \sim 1.25^\circ$). While the results formally indicate that the metal-richer stars are more centrally concentrated, the statistical significance is not conclusive. Forthcoming papers based on reductions of the rest of our dataset will address this question more extensively.

5. Discussion

Our derived M31 MDF in total (Figure 9) shows a strong, rather narrow peak at $[m/H] \sim -0.5$ (corresponding to $[Fe/H] \sim -0.8$), and an extended metal-poor tail. The dominant high-metallicity peak has been seen in most previous photometric studies (which surveyed fields located from 7 to 20 kpc from the M31 nucleus) to date, although the derived dispersion about the mean $[Fe/H]$ has varied considerably. Mould & Kristian (1986) found $[Fe/H] \sim -0.6$, while Christian & Heasley (1991) found the halo to have a metallicity similar to that of 47 Tuc; both studies suggested a significant metallicity spread. Pritchet & van den Bergh (1988) and Davidge (1993) both found a mean $[Fe/H] \sim -1^4$, with a smaller metallicity dispersion $\sigma \sim 0.3$ dex. Durrell, Harris & Pritchet (1994) derived $[Fe/H] \sim -0.6$, with a similarly small $\sigma \sim 0.3$ dex. Couture et al. (1995) also found a rather metal-rich halo ($[Fe/H] \sim -0.5$, $\sigma \sim 0.5$). Holland, Fahlman & Richer (1996) showed that the M31 halo MDF is asymmetric, with a peak at $[Fe/H] \sim -0.6$, but where stars had $-2 < [Fe/H] < -0.2$. Finally, Reitzel, Guhathakurta & Gould (1998) concluded the M31 halo has $[Fe/H] < -1$ based on their photometry of the 20 kpc field (similar location as our $\mathcal{M}2$ field). All studies (with the exception of Durrell, Harris & Pritchet 1994) based their metallicity estimates on the location of globular cluster RGBs, and in particular with that of 47 Tucanae, which has $[Fe/H] \sim -0.7$ ⁵. This observed peak in our MDF is very similar to that of other studies, and strengthens the conclusion that a large metallicity gradient does *not* exist in the M31 halo at $r_{M31} \sim 7 - 20$ kpc.

However, the metal-poor tail in our MDF is also strong, and our preceding analysis indicates that it *cannot* be explained as AGB contamination from the metal-rich population. While most early studies focussed primarily on the mean $[Fe/H]$ of the *entire* halo population and the consequent high dispersion σ about this mean, it is clear that such a description covers over many of the details in the MDF. We will explore how the MDF gives us some clues as to the origin of the M31 halo via

⁴The lower value of $[Fe/H] = -1$ from Pritchet & van den Bergh (1988) is due to their use of a V limit to their V , $(B - V)$ CMD. For the tip of the RGB, M_V decreases as metallicity increases, and their chosen cutoff would have been biased against higher- $[Fe/H]$ stars.

⁵Note that in the RGB calibration scheme of Harris & Harris (2000) [which is adopted in this paper] 47 Tucanae is found to have $[m/H] \sim -0.63$, or $[Fe/H] \sim -0.94$; which is very close to that of our metal-rich peak. As most M31 halo studies have compared directly to the 47 Tuc RGB, there is *strong* agreement between our results and all previous work.

comparisons with the globular cluster system, and with predictions from simple models of galactic chemical evolution. We will also compare our results to those from two elliptical galaxies for which MDFs have been derived from resolved stellar populations: NGC 5128 (Harris, Harris & Poole 1999; Harris & Harris 2000) and M32 (Grillmair et al. 1996).

5.1. Halo or Bulge?

The presence of a strong metal-rich population in the outer regions of M31 has raised the question whether or not we are looking at a true ‘halo’ population (as assumed by many works, including Mould & Kristian 1986; Durrell, Harris & Pritchett 1994; Holland, Fahlman & Richer 1996, and the current study, to name but a few), or an outward extension of the rather large ‘bulge’ of M31 (Bica, Barbuy & Ortolani 1991; Freeman 1996).

While difficult to study because of intense crowding, the M31 nuclear (or inner) bulge is similar to that of the MW in that it seems to be dominated by old stars of roughly solar metallicity (Renzini 1999; Jablonka et al. 1999, 2000). Of note here is that the numerous M31 halo studies to date (including the present study) do *not* find the Solar-metallicity stars that make up the inner bulge population. The mean $[m/H]$ in the bulge populations suggests a rather strong metallicity gradient (~ 0.1 dex/kpc or more) in the M31 bulge, while the relative uniformity of the mean metallicity of the *halo* population at $r_{M31} = 7 - 20$ kpc suggests that such a gradient does not continue beyond the inner bulge (Pritchett & van den Bergh 1988; Rich et al. 1996b, and the discussion above).

However, it is known that the $r^{1/4}$ nature of the inner bulge continues out to $r = 20$ kpc (PvdB94). Thus it becomes difficult to simply define a clear ‘bulge’ and ‘halo’ in terms similar to that of the Milky Way. It seems likely that we are actually observing a continuum of populations in the M31 *spheroid* – a $Z \sim Z_{\odot}$ population in the central regions and somewhat more metal-poor in the outer reaches. That the same distribution holds well for the entire observed range to date lends credence to the possibility that the formation of the metal-rich ‘bulge’ or inner spheroid is strongly related to the formation (or the aftermath) of the ‘halo’ or outer spheroid. Studies of the MDF of stars in the region $r_{M31} = 2 - 7$ kpc (and similar radii in other large spheroids) could prove quite interesting in pinning down this metallicity gradient, and assist in understanding the origin of bulges/spheroids in M31 and other galaxies.

Based on this limited information, we are led to conclude that our 20-kpc field is almost entirely ‘halo’ rather than ‘bulge’ (in the traditional sense), but perhaps more correctly called the ‘outer spheroid’.

5.2. Comparison with the Globular Cluster System

M31 possesses a large (> 400) population of globular clusters which has been the focus of many metallicity-based studies (Huchra, Brodie & Kent 1991, and references within). Recently, Barmby et al. (2000) completed a large catalog of spectroscopically- and photometrically- derived metallicities of the M31 GCS and found its metallicity distribution to be roughly bimodal (seen also by Huchra, Brodie & Kent 1991; Ashman & Bird 1993), with peaks in the distribution at $[\text{Fe}/\text{H}] \sim -1.4$ and $[\text{Fe}/\text{H}] \sim -0.6$. In this sense the M31 halo resembles the bimodal GC distribution in the MW (Zinn 1985; Harris 2000), with the metal-poor ‘halo’ component and the more metal-rich ‘bulge’ subsystem (Minniti 1995; Barbuy, Bica & Ortolani 1998; Côté 1999; Barmby et al. 2000) at very similar mean metallicity values. Both Barmby et al. (2000) and Huchra, Brodie & Kent (1991) also found a *small* $[\text{Fe}/\text{H}]$ -gradient in the population, with the tendency for the most metal-rich GCs to lie at smaller r_{M31} .

Figure 13 shows a plot of our field MDF with that of all M31 GCs with spectroscopically determined metallicity values ($N = 188$) from Barmby et al. (2000) (we have applied $[\text{m}/\text{H}] = [\text{Fe}/\text{H}] + 0.3$ to the Barmby et al. results). While we have used GCs at all radii around M31 for comparison, the lack of any strong metallicity gradient in the M31 GCS indicates this is an acceptable choice. What is seen is that *both* the globular clusters and field stars span the complete range $-2.2 < [\text{m}/\text{H}] < -0.2$ (see also Reitzel & Guhathakurta 2001). However, the most striking feature of Figure 13 is that the two distributions have emphatically different shapes: far more GCs are metal-poor, while a far larger fraction of bulge/halo field stars are metal-rich. From Barmby et al. (2000), 34% of the GCs (of those that could be confidently assigned to one population or the other) are ‘bulge’ (ie. metal-rich) clusters, while we find that $\sim 60\%$ of the field stars have a similar $[\text{m}/\text{H}]$.

This comparison suggests that the *specific frequency* S_N (number of GCs per unit halo luminosity; Harris & van den Bergh 1981) is about three times larger for the metal-poor population than for the metal-rich population. A very similar result was found by Harris, Harris & Poole (1999) for the dual-component GCS and halo in the giant elliptical NGC 5128. *If* the GCs and halo stars in the same metallicity range are generically related, this comparison suggests either (a) the formation efficiency of the metal-rich clusters was lower, or (b) the formation efficiency of the metal-poor *stars* was lower, relative to the number of globular clusters formed. We will return to this point below. This comparison of course ignores the possible effects of dynamical evolution and destruction of clusters in the inner regions of M31, but the differences in destructive efficiency between metal-rich and metal-poor clusters would have to be dramatic indeed to produce the factor-of-three difference that we now observe.

As noted earlier (eg. Durrell, Harris & Pritchett 1994; Holland, Fahlman & Richer 1996) the M31 halo MDF *on average* is much more metal-enriched than the GCS (by ~ 0.3 dex, typical of that seen in other galaxies, Harris 2000). The difference is now much more subtle with the expanded datasets, and is complicated by the possible relation between the GCs and field stars in

each metallicity component. The M31 halo clusters appear to have a more extended distribution than the M31 bulge clusters (Huchra, Brodie & Kent 1991; Barmby et al. 2000), and there is a hint of a similar situation for the two ‘components’ of the halo star population (see section 4.2 above). There may also be kinematic differences between the metal-rich and metal-poor GC subsystems out to 15 kpc (Huchra, Brodie & Kent 1991; Barmby et al. 2000). It is plausible the GCs and stars in each metallicity subsystem are directly related, but kinematical studies of both the GCs *and* halo stars will be of the utmost importance in solving this issue – such efforts are currently underway (Perrett et al. 2000; Reitzel & Guhathakurta 2001).

5.3. Chemical Evolution Models

We will now describe the MDF using simple models of galactic chemical evolution. Here, we abandon the rather artificial division between “metal-rich” and “metal-poor” parts of the stellar population that we used above for comparative purposes, and treat the MDF as a whole. We ask here the straightforward question how well the Simple (closed-box) Model of chemical evolution (eg. Searle & Sargent 1972; Pagel & Patchett 1975) applies to the M31 halo. In this model, the cumulative $N(Z)$ (number of stars with abundance lower than Z) follows

$$N(Z) \propto \frac{1 - e^{-(Z-Z_0)/y}}{1 - e^{-(Z_{now}-Z_0)/y}} \quad (5)$$

where Z_0 is the initial abundance of the gas in the “box”, Z_{now} is the present-day abundance, and y is the yield due to nucleosynthesis. The differential distribution dN/dZ will show an exponential decay with increasing Z . If we allow metal-enriched gas to leave the system, expelled by supernova-driven winds (the ‘leaky-box’ model of Hartwick 1976, see also Searle & Zinn 1978, Binney & Merrifield 1998), then the true yield y is reduced to the ‘effective yield’ $y_{eff} = y/(1 + c)$, where c is a parameter that describes the fraction of gas mass lost from the box, but the exponential form of dN/dZ remains the same.

Since the Simple model is so well suited to the linear differential abundance distribution, we choose to plot the MDF this way rather than in the more traditional logarithmic form as in Fig. 9. This form of the MDF is plotted in Figure 14. We have assumed $Z_\odot = 0.0172$ and $[\alpha/Fe] = +0.3$ throughout, though these assumptions will have little bearing on the discussion to follow.

In Figure 14 we have plotted the expected curves for Simple models with Z_0 and various choices of y_{eff} , chosen to illustrate what the model would predict over the observed range in Z . Three features of this comparison immediately emerge:

(a) The model, in broad terms, matches the M31 data for the entire run $0.0 < Z/Z_\odot < 0.8$. Notably, the number of observed stars at the lowest abundances continue to rise towards $Z \rightarrow 0$ in the roughly exponential form required by the model. In some other galaxies (see especially Harris & Harris 2000 for the case of NGC 5128) the lowest-metallicity stars are conspicuous by their near-

absence, and the differential distribution dN/dZ actually declines near $Z \rightarrow 0$, deviating strongly from the exponential-decay condition.

(b) The best-fit effective yield for the M31 halo is 5 to 6 times larger than for the Milky Way halo, for which best-fit values are in the range $y_{eff} \sim 0.0009$ (Ryan & Norris 1991). If the intrinsic nucleosynthetic yield y for the two galaxies was at all similar in their earliest star-forming stages, then (within the context of the same chemical enrichment models) the M31 halo must have successfully held on to a much higher fraction of its gas, allowing the enrichment to proceed up to higher levels.

(c) There is an excess of *intermediate-metallicity* stars with $Z \sim 0.3 - 0.5Z_{\odot}$. Comparisons of the cumulative $N(Z)$ distributions with the enrichment models through a standard Kolmogorov test show that the data differ from the models with a significance higher than 99%, regardless of choice of y_{eff} . That is, the Simple model matches the data to first order, but fails to describe the MDF in detail.

It would have been plausible to expect that the most natural comparison for the M31 MDF is the halo of the Milky Way, which is a basically similar galaxy type. Instead, the M31 halo even in its outer regions clearly does not resemble the Milky Way at all, but rather the MDFs of elliptical galaxies such as NGC 5128 (Harris & Harris 2000) or M32 (Grillmair et al. 1996). In Figure 15, we plot our M31 MDF with the combined MDFs for the outer halo of NGC 5128 ($r \sim 20$ to 30 kpc, closely comparable to our M31 field) derived by Harris & Harris (2000) with the same RGB models and interpolation technique. Both MDFs show a dominant metal-rich peak ($[m/H] \sim -0.5$ for M31, ~ -0.4 for NGC 5128) with a long metal-poor tail. In detail, we see that the NGC 5128 MDF extends to slightly higher metallicity at the top end, and has noticeably fewer stars at the low end. Harris & Harris (2000) suggest that a two-phase chemical evolution model is needed to explain the NGC 5128 MDF: an early “accreting box” stage during which unenriched gas continued to flow in to the protogalaxy while it was going through its first rounds of star formation, until the overall abundance had built up to $Z \simeq 0.25Z_{\odot}$; and then a second stage after the gas infall died away and the system approached a standard closed-box evolution. During this latter stage, the effective yield for the outer NGC 5128 halo is $y \simeq 0.006$, quite similar to what we see in M31. Thus for M31, invoking this first phase of combined star formation *with gas accretion* at very early times seems not to be necessary.

Our M31 MDF is also quite similar in form to the MDF of the low-luminosity compact elliptical galaxy M32 (Grillmair et al. 1996). Just as for NGC 5128, M32 has extremely few low-metallicity stars. We note, however, that the M32 MDF was drawn from a sample close to the nuclear regions, while the NGC 5128 and M31 MDFs are from much further out in the halo; (see the comments by Grillmair et al. 1996, on the possibility of lower-metallicity stars lying at larger r from M32). In sum, however, the material from these three galaxies is rather suggestive of a common formation mechanism for massive spheroids (elliptical galaxies and large bulges), despite differences in the details.

5.4. Formation of the M31 Halo

Hierarchical models of galaxy formation provide a plausible physical basis for how galaxies form (eg. Cole et al. 1994; Kauffmann 1996; Klypin et al. 1999; Côté et al. 2000a). In this context, we expect the metal-poor M31 halo to have formed from the agglomeration of protogalactic, dwarf-sized clouds (Searle & Zinn 1978; Harris & Pudritz 1994), each of which had likely formed some proportion of stars and globular clusters before they began amalgamating into the M31 halo. Furthermore, the observations thus far are consistent with the M31 halo and bulge (spheroid) being composed *predominantly of old stars* and that the bulk of star formation took place at very early times, during the hierarchical assembly. The models of Côté et al. (2000a) show that such a mechanism does an excellent job of explaining the metallicity distributions of both the halo globular clusters and halo field stars in the Milky Way, provided that the luminosity function of the incoming fragments is $dn/dL \propto L^{-2}$ and there is no dissipation of the gas. To explain the more metal-rich M31 halo, they suggest a slightly flatter mass spectrum $\sim L^{-1.8}$ for the fragments to allow more massive fragments (with their decidedly more metal-rich stars) to contribute more to the halo. However, enough metal-poor stars are still formed to match the numbers that we observe, so that it does not seem necessary to invoke significant additional accretion of primarily stellar material (dwarf ellipticals) at later times.

On the other hand, it may be necessary to invoke a special explanation for the stars at $Z \simeq 0.3 - 0.5Z_{\odot}$, i.e. the ones forming the peak of the MDF in Fig. 13. Their excess of numbers over the standard chemical evolution models is highly significant. These stars are far too metal-rich to have been acquired from (e.g.) dwarf elliptical galaxies or any low-mass fragments with small potential wells, and their presence may suggest that a particularly large “fragment” or partially evolved massive satellite was acquired early on.

Another puzzle is the contrast in globular cluster specific frequency between the metal-poor and metal-rich ends of the MDF. The answer may lie in when and where each type of globular cluster formed. As suggested by Harris, Harris & Poole (1999) for the clearly similar case of NGC 5128, one possibility for understanding the much higher S_N for metal-poor clusters is to suppose that the gaseous protoclouds merged together just *after* most of them had formed (metal-poor) globular clusters, but *before* much of their local star formation had taken place. That is, globular cluster formation (logically, in the very densest parts of the protoclouds) would occur earliest of all, and the supernova-driven winds might have truncated star formation in the rest of their local parent clouds. Later on, the bulk of the gas – now mostly merged into the M31 protohalo – would then have continued to form progressively more metal-rich stars in the considerably larger, deeper potential well of M31, along with the majority of metal-rich globular clusters.

If the basic hierarchical merger model is correct, then the S_N pattern we have noted here should be a common property of giant galaxies. These speculations should be tested with additional data from other such galaxies. Furthermore, as mentioned above, kinematics of both halo stars and the globular clusters are crucial to understanding both the M31 bulge and halo. If the above scenario

is correct, we would expect the metal-rich stars *and* GCs to have rather similar kinematics. If the collapse of the gas expelled by the halo stars was dissipative, the metal-rich stellar populations should be rotating, but slower than stars in the inner (nuclear) bulge. As for the metal-poor halo component of M31, the true rotation and velocity dispersion will depend (somewhat) on the contributions from later accretion, but should be noticeably less than that of the metal-rich component. As noted, this appears to be the case for the globular cluster system (Huchra, Brodie & Kent 1991; Barmby et al. 2000).

The question still remains why the M31 halo is *on average* so much more metal-rich than that of the Milky Way halo, even though the MDF shapes are both approximately described by Simple models of chemical evolution. As other authors have discussed (cf. the references cited earlier), the Milky Way halo distribution is suggestive of the idea that almost all its halo stars were formed within dwarf-sized units with small potential wells, which could sustain only very low effective yields, and that these small systems amalgamated later with relatively little subsequent star formation. In M31, it seems much more necessary to propose that *a very large fraction of the star formation took place only after the gaseous fragments had merged*, so that the gas could remain within the much larger potential well of the entire giant galaxy, and drive upward to higher metallicity. In this sense, the formation of the M31 halo appears to resemble that of a giant elliptical.

6. Summary

As part of our survey of the M31 halo, we have presented ($I, V - I$) photometry from a field located 20 kpc from the galaxy center along the SE minor axis and also a remote background field. Using image classification and comparison with the background field, we have been able to isolate a sample of several thousand M31 halo stars, from which we derive a TRGB-based distance modulus $(m - M)_0 = 24.47 \pm 0.12$ ($d = 783 \pm 43$ kpc). There are no statistically significant numbers of M31 halo stars brighter than the classic old-halo RGB tip, consistent with the interpretation that we are looking at a homogeneous, old stellar population. Reddening estimates for our fields are $E(V - I) = 0.10 \pm 0.02$ for $\mathcal{M}2$ and 0.08 ± 0.02 for the background $\mathcal{R}1$ field, found from the colors of foreground Milky Way halo stars in the color-magnitude diagrams.

Using a dense grid of RGB stellar models, we derive the metallicity distribution function for the outer M31 halo. The MDF contains stars of a wide range of $[m/H]$, but with a distinct peak at $[m/H] \sim -0.54$. There is no evidence for a significant population of stars with $[m/H] > -0.3$ at this location of the M31 bulge/halo. A single “Simple model” of chemical evolution does match the MDF to first order, but with some clear second-order deviations. The effective yield best matching the MDF ($y_{eff} \simeq 0.0055$) is about 6 times higher than that for the Milky Way halo; instead, it more closely resembles the MDFs for the halos of the elliptical galaxies NGC 5128 and M32.

We outline a scenario for the formation of the M31 halo based on contemporary models for hierarchical merging of protogalactic gas clouds:

– The earliest star formation took place within these dwarf-sized gas clouds clearly before they merged, during which time the metal-poor globular clusters and some metal-poor stars formed.

– Agglomeration of these fragments into the global halo of M31 occurred while the fragments were primarily gaseous, The (mainly) gaseous proto-halo then proceeded to form most of its stars (as well as most of the metal-rich globular clusters). Most of the gas was held within the deep, massive potential well of the giant galaxy, allowing the gas to evolve up to high metallicity roughly according to the closed-box chemical evolution model.

– Some fraction of the now-enriched halo gas may have found its way inward to help form the still more metal-rich population in the inner bulge ($r < \text{a few kpc}$). Although the timescale of this stage is not constrained by our data, it is expected to be not long after the halo formation itself, resulting in the formation of old, solar metallicity stars that populate the inner bulge.

This project has benefited greatly from fruitful discussions with Tim Davidge, Pat Côté, Steve Holland, Raja Guhathakurta, Steve Majewski, Harvey Richer, Greg Fahlman, Stéphane Courteau, Peter Bergbusch, Don VandenBerg, and David Hartwick. This research was supported by NSERC research grants to WEH and CJP, and PRD gratefully acknowledges financial support from Robin Ciardullo, Harvey Richer, and Greg Fahlman. We also acknowledge use of facilities made available by the Canadian Astronomy Data Centre, which is operated by the Herzberg Institute of Astrophysics, National Research Council of Canada.

REFERENCES

- Ashman, K.M., & Bird, C.M. 1993, AJ, 106, 2281
- Barbuy, B., Bica, E., & Ortolani, S. 1998, A&A, 333, 117
- Barmby, P., Huchra, J.P., Brodie, J.P., Forbes, D.A., Schroder, L.L., & Grillmair, C.J. 2000, AJ, 119, 727
- Beers, T.C., Wilhelm, R., Doinidis, S.P., & Mattson, C.J. 1996, ApJS, 103, 433
- Bertelli, G., Bressan, A., Chiosi, C., Fagotto, F., & Nasi, E. 1994, A&AS, 106, 275
- Bica, E., Barbuy, B., & Ortolani, S. 1991, ApJ, 382, L15
- Binney, J., & Merrifield, M. 1998, Galactic Astronomy (Princeton: Princeton University Press), 311
- Burstein, D., & Heiles, C. 1984, ApJS, 54, 33
- Cardelli, J.A., Clayton, G.C., & Mathis, J.S. 1989, ApJ, 345, 245

- Carney, B.W., Laird, J.B., Latham, D.W., & Aguilar, L.A. 1996, *AJ*, 112, 668
- Christian, C.A., & Heasley, J.N. 1991, *AJ*, 101, 848
- Cole, S., Aragon-Salamanca, A., Frenk, C.S., Navarro, J.F., & Zepf, S.E. 1994, *MNRAS*, 271, 781
- Côté, P. 1999, *AJ*, 118, 406
- Côté, P., Marzke, R.O., West, M.J., & Minniti, D. 2000, *ApJ*, 533, 869
- Côté, P., Mateo, M., Sargent, W.L.W., & Olszewski, E.W. 2000, *ApJ*, 537, 91
- Courteau, S., & van den Bergh, S. 1999, *AJ*, 118, 337
- Couture, J. Racine, R., Harris, W.E., & Holland, S. 1995, *AJ*, 109, 2050
- Da Costa, G. S., & Armandroff, T.E. 1990, *AJ*, 100, 162
- Davidge, T. 1993, *ApJ*, 409, 190
- Durrell, P.R., Harris, W.E., & Pritchett, C.J. 1994, *AJ*, 108, 2114
- Evans, N.W., & Wilkinson, M.I. 2000, *MNRAS*, 316, 929
- Ferrarese, L., et al. 2000, *ApJ*, 529, 745
- Fleming, D.E.B., Harris, W.E., Pritchett, C.J., & Hanes, D.A. 1995, *AJ*, 109, 1044
- Freeman, K.C. 1996, in the *Formation of the Galactic Halo...Inside and Out*, eds. H.Morrison & A.Sarajedini, *ASP Conf. Ser.*, 92, 3
- Freeman, K.C. 1999, in the *Third Stromlo Symposium: The Galactic Halo*, eds. B.K. Gibson, T.S. Axelrod, and M.E. Putman, *ASP Conf. Ser.*, 165, 167
- Gallart, C. 1998, *ApJ*, 495, L43
- Girardi, L., Bressan, A., Bertelli, G., & Chiosi, C. 2000, *A&AS*, 141, 371
- Grillmair, C.J., et al. 1996, *AJ*, 112, 1975
- Harris, G.L.H., & Harris, W.E. 2000, *AJ*, 120, 2423
- Harris, G.L.H., Harris, W.E., & Poole, G.B. 1999, *AJ*, 117, 855
- Harris, W.E., & van den Bergh, S. 1981, *AJ*, 86, 1627
- Harris, W.E., Fitzgerald, M.P., & Reed, B.C. 1981, *PASP*, 93, 507
- Harris, W.E., Allwright, J.W.B., Pritchett, C.J., & van den Bergh, S. 1991, *ApJS*, 76, 115

- Harris, W.E., & Pudritz, R.E. 1994, *ApJ*, 429, 177
- Harris, W.E., Durrell, P.R., Pierce, M.J., & Secker, J. 1998, *Nature*, 395, 45
- Harris, W.E. 2000, in *Star Clusters*, Saas-Fee Advanced Course 28, Swiss Society for Astrophysics & Astronomy (Springer-Verlag)
- Hartwick, F.D.A. 1976, *ApJ*, 209, 418
- Helmi, A., et al. 1999, *Nature*, 402, 53
- Holland, S. 1998, *AJ*, 115, 1916
- Holland, S., Fahlman, G.G., & Richer, H.B. 1996, *AJ*, 112, 1035
- Huchra, J.P., Brodie, J.P., & Kent, S.M. 1991, *ApJ*, 370, 495
- Ibata, R., Irwin, M., Lewis, G.F., & Stolte, A. 2000, *ApJ*, submitted
- Ivezic, Z., et al. 2000, *AJ*, 120, 963
- Jablonka, P., Bridges, T.J., Sarajedini, A., Meylan, G., Maeder, A., & Meynet, G. 1999, *ApJ*, 518, 627
- Jablonka, P., Courbin, F., Meylan, G., Sarajedini, A., Bridges, T.J., & Magain, P. 2000, *A&A*, 359, 131
- Johnson, J.A., & Bolte, M. 1998, *AJ*, 115, 693
- Kauffmann, G. 1996, *MNRAS*, 281, 487
- Kron, R.G. 1980, *ApJS*, 43, 305
- Klypin, A., Kravtsov, A.V., Valenzuela, O., & Prada, F. 1999, *ApJ*, 522, 82
- Landolt, A.U. 1992, *AJ*, 104, 340
- Majewski, S.R., Ostheimer, J.C., Kunkel, W.E., & Patterson, R.J. 2000, *AJ*, 120, 2550
- McLaughlin, D.E., Secker, J., Harris, W.E., & Geisler, D. 1995, *AJ*, 109, 1033
- Minniti, D. 1995, *AJ*, 109, 1663
- Morrison, H.L. 1999, in the *Third Stromlo Symposium: The Galactic Halo*, eds. B.K. Gibson, T.S. Axelrod, and M.E. Putman, *ASP Conf. Ser.*, 165, 174
- Morrison, H.L., Mateo, M., Olszewski, E.W., Harding, P., Dohm-Palmer, R.C., Freeman, K.C., Norris, J.E., & Morita, M. 2000, *AJ*, 119, 2254

- Mould, J. 1986, in *Stellar Populations*, ed. C.A.Norman, A.Renzini, & M.Tosi (Cambridge: Cambridge University Press), 9
- Mould, L., & Kristian, J. 1986, *ApJ*, 305, 591
- Pagel, B.E.J., & Patchett, B.E. 1975, *MNRAS*, 172, 13
- Perrett, K., Hanes, D., Bridges, T., Irwin, M., Carter, D., Huchra, J., Brodie, J., & Watson, F. 2000, *BAAS*, 196, 2803
- Pritchett, C.J., & van den Bergh, S. 1987, *ApJ*, 316, 517
- Pritchett, C.J., & van den Bergh, S. 1988, *ApJ*, 331, 135
- Pritchett, C.J., & van den Bergh, S. 1994, *AJ*, 107, 1730 (PvdB94)
- Reitzel, D.B., Guhathakurta, P., & Gould, A. 1998, *AJ*, 116, 707
- Reitzel, D.B., & Guhathakurta, P. 2001, in preparation
- Renzini, A. 1999, in *When and How do Bulges Form and Evolve?*, edited by C.M. Carollo, H.C.Ferguson & R.F.G. Wyse (Cambridge : Cambridge University Press), 9
- Rich, R.M., Mighell, K.J., Freedman, W.L., & Neill, J.D. 1996, *AJ*, 111, 768
- Rich, R.M., Mighell, K.J., & Neill, J.D. 1996, in *the Formation of the Galactic Halo...Inside and Out*, eds. H.Morrison & A.Sarajedini, *ASP Conf. Ser.*, 92, 544
- Ryan, S.G., & Norris, J.E. 1991, *AJ*, 101, 1865
- Sandquist, E.L., Bolte, M., Langer, G.E., Hesser, J.E., & de Oliveira, C.M. 1999, *ApJ*, 518, 262
- Schlegel, D.J., Finkbeiner, D.P., & Davis, M. 1998, *ApJ*, 500, 525
- Searle, L, & Sargent, W.L.W. 1972, *ApJ*, 173, 25
- Searle, L., & Zinn, R. 1978, *ApJ*, 225, 357
- Sommer-Larsen, J., Beers, T.C., Flynn, C., Wilhelm, R., & Christensen, P.R. 1997, *ApJ*, 481, 775
- Stanek, K.Z., & Garnavich, P.M. 1998, *ApJ*, 503, L131
- Stetson, P.B. 1987, *PASP*, 99, 191
- Stetson, P.B., Davis, L.E., & Crabtree, D.R. 1990, in *CCDs in Astronomy*, ed. G.H. Jacoby, *ASP Conf. Ser.*, 8, 289
- Stetson, P.B. 1992, in *Astronomical Data Analysis Software and Systems I*, eds. D.M. Worrall, C. Biemesderfer, and J. Barnes, *ASP Conf. Ser.*, 25, 297

Totten, E.J., & Irwin, M.J. 1998, MNRAS, 294, 1

VandenBerg, D.A., Swenson, F.J., Rogers, F.J., Iglasias, C.A., & Alexander, D.R. 2000, ApJ, 532, 452

van den Bergh, S. 1991, PASP, 103, 1053

van den Bergh, S., & Pritchett, C.J. 1992, in *The Stellar Populations in Galaxies*, ed. B.Barbuy & A. Renzini (Dordrecht: Kluwer), 161

Wyse, R.F.G., Gilmore, G., & Franx, M. 1997, ARA&A, 35, 637

Yanny, B., Newberg, H.J., et al. 2000, ApJ, 540, 825

Zinn, R. 1985, ApJ, 273, 424

Table 1. Limiting Magnitudes

CCD #	$\mathcal{M}2$		$\mathcal{R}1$	
	V_{lim}	I_{lim}	V_{lim}	I_{lim}
0	24.12	23.90	24.86	23.74
1	24.31	24.03	24.96	23.88
2	24.11	23.67	24.77	23.47
3	24.36	23.95	24.94	23.72
5	24.37	23.96	24.93	23.79
7	23.94	23.77	24.60	23.53

Table 2. Metallicity Distribution Function

[m/H]	$\mathcal{M}2$		$\mathcal{R}1^a$		$\mathcal{M}2 - \mathcal{R}1$	
	N_c	σ	N_c	σ	N_c	σ
–2.30	4.8	2.4	0.0	0.0	4.8	2.4
–2.20	14.7	4.1	1.1	1.1	13.7	4.2
–2.10	26.6	5.4	7.5	2.8	19.1	6.1
–2.00	32.1	6.0	8.5	3.0	23.6	6.7
–1.90	56.6	7.8	6.4	2.6	50.3	8.2
–1.80	44.8	7.0	4.2	2.1	40.5	7.3
–1.70	55.8	7.7	3.2	1.8	52.7	8.0
–1.60	51.5	7.5	7.5	2.8	44.0	8.0
–1.50	82.8	9.4	12.8	3.7	70.0	10.1
–1.40	82.1	9.4	13.8	3.8	68.3	10.2
–1.30	92.6	10.0	11.7	3.5	80.9	10.6
–1.20	99.3	10.4	14.0	3.9	85.3	11.0
–1.10	155.9	12.9	17.1	4.3	138.8	13.6
–1.00	138.4	12.1	20.3	4.7	118.1	13.0
–0.90	213.7	15.1	24.5	5.1	189.1	15.9
–0.80	231.8	15.8	29.9	5.7	201.9	16.8
–0.70	272.8	17.4	40.7	6.6	232.2	18.6
–0.60	365.8	21.0	69.5	8.6	296.3	22.7
–0.50	455.8	25.9	81.2	9.4	374.5	27.5
–0.40	421.1	24.6	104.8	10.7	316.3	26.9
–0.30	351.7	22.6	144.1	12.5	207.6	25.9
–0.20	299.2	22.9	166.9	13.7	132.3	26.7
–0.10	208.1	23.0	167.8	14.3	40.3	27.1

^acounts corrected to area of $\mathcal{M}2$ field

Table 3. Dual-Gaussian fit to MDF

	metal-rich peak	metal-poor peak
[m/H]	-0.520 ± 0.008	-1.195 ± 0.055
σ	0.203 ± 0.009	0.450 ± 0.027
proportions	0.598 ± 0.037	0.402 ± 0.037

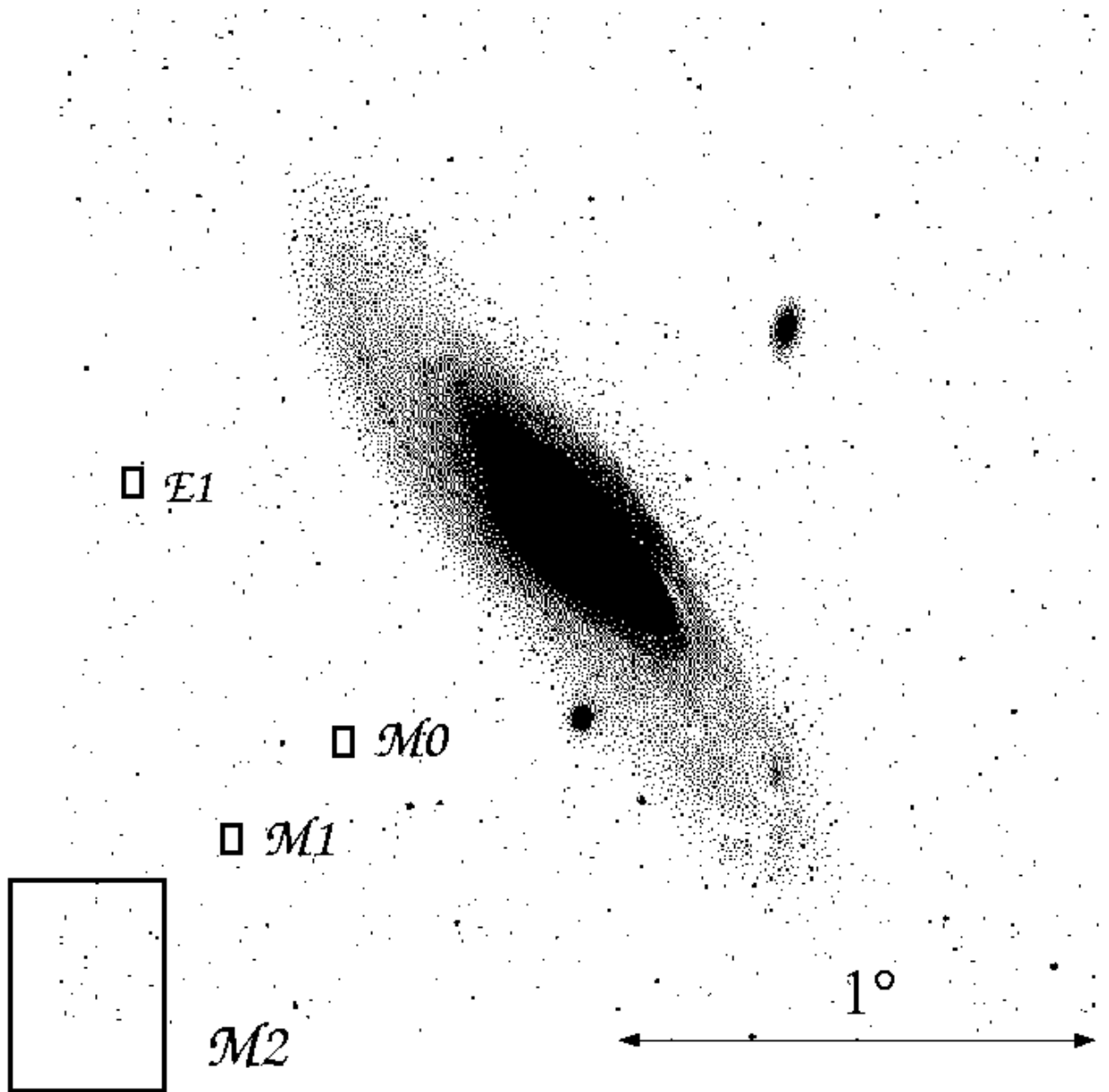


Fig. 1.— Location of the M31 halo field ($\mathcal{M}2$) under study in this paper – the field size is that of the usable area of the UH8K mosaic ($21' \times 28'$). The smaller $2' \times 3'$ fields represent the fields studied previously by Pritchett and van den Bergh (1994). M31 image courtesy Bill Schoening, Vanessa Harvey /REU program/AURA/NOAO/NSF.

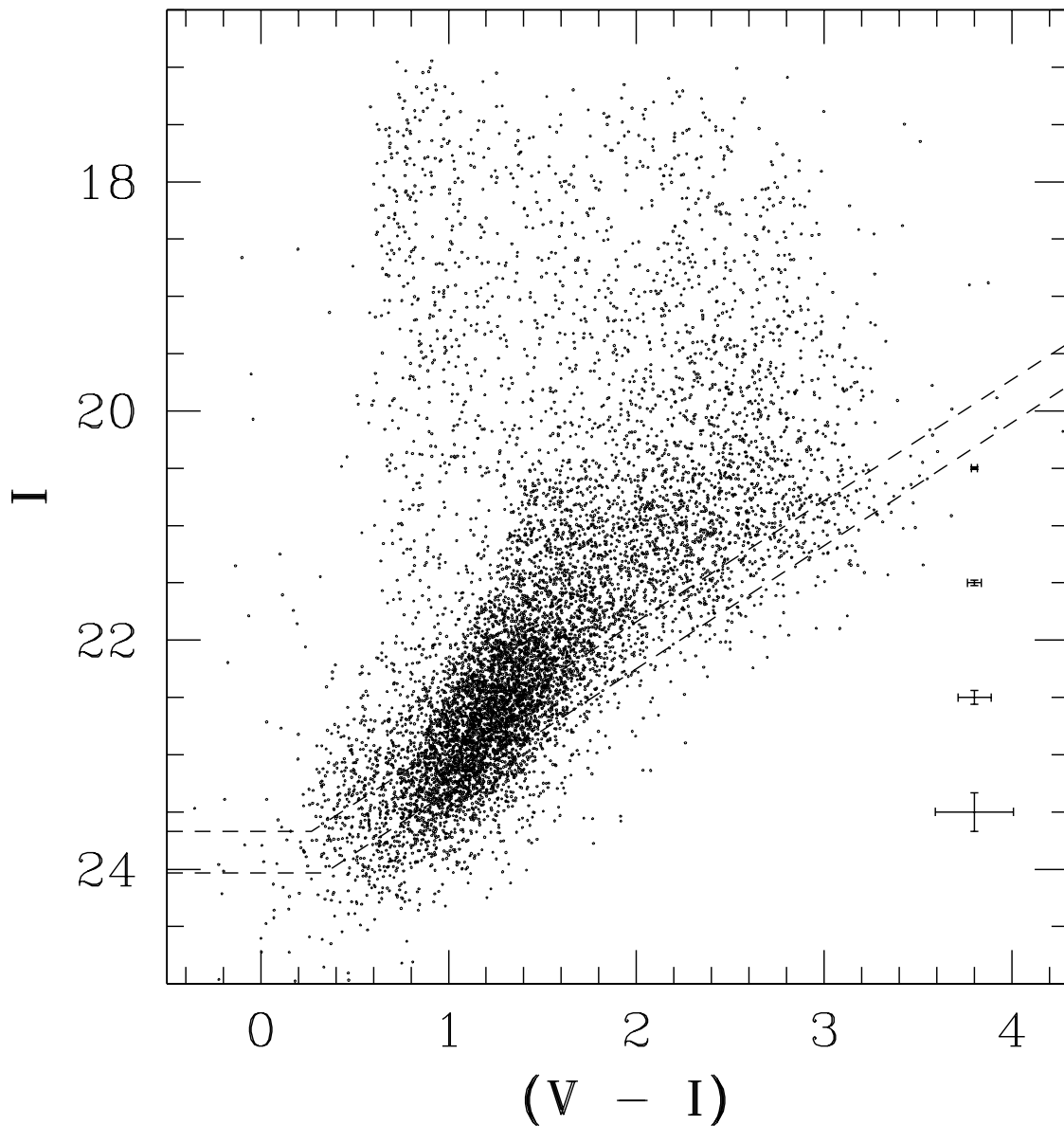


Fig. 2.— VI Color magnitude diagram of the $\mathcal{M}2$ halo field, based on data from all 6 usable chips of the CCD array. The dashed lines denote the full range of the 50% completeness levels for the CCDs used. All non-stellar objects have been rejected via image classification. The plotted error bars denote the *representative* errors for objects with $(V - I) = 1$.

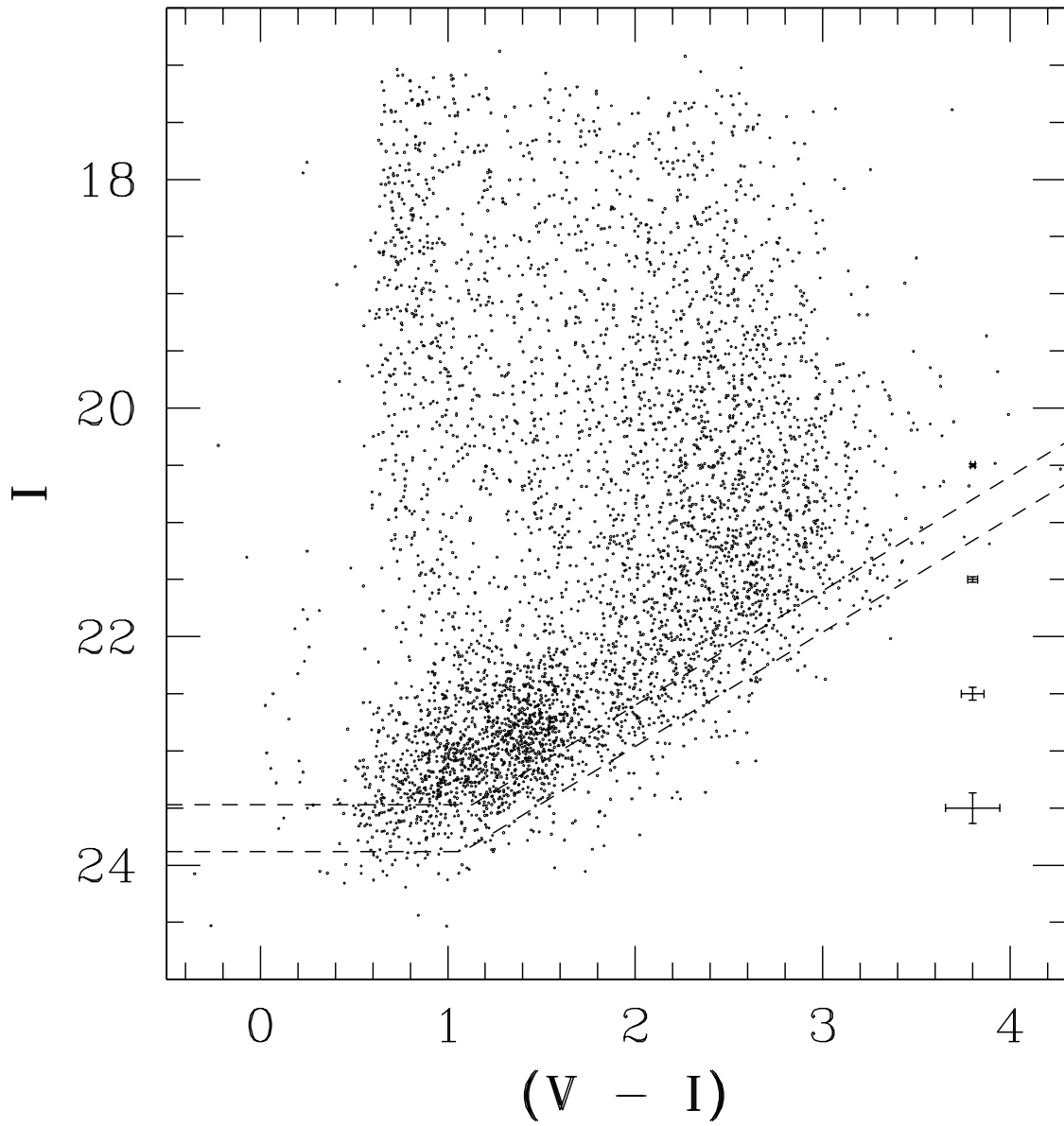


Fig. 3.— Color-magnitude diagram of the background $\mathcal{R}1$ field. Lines are same as those plotted in Figure 2.

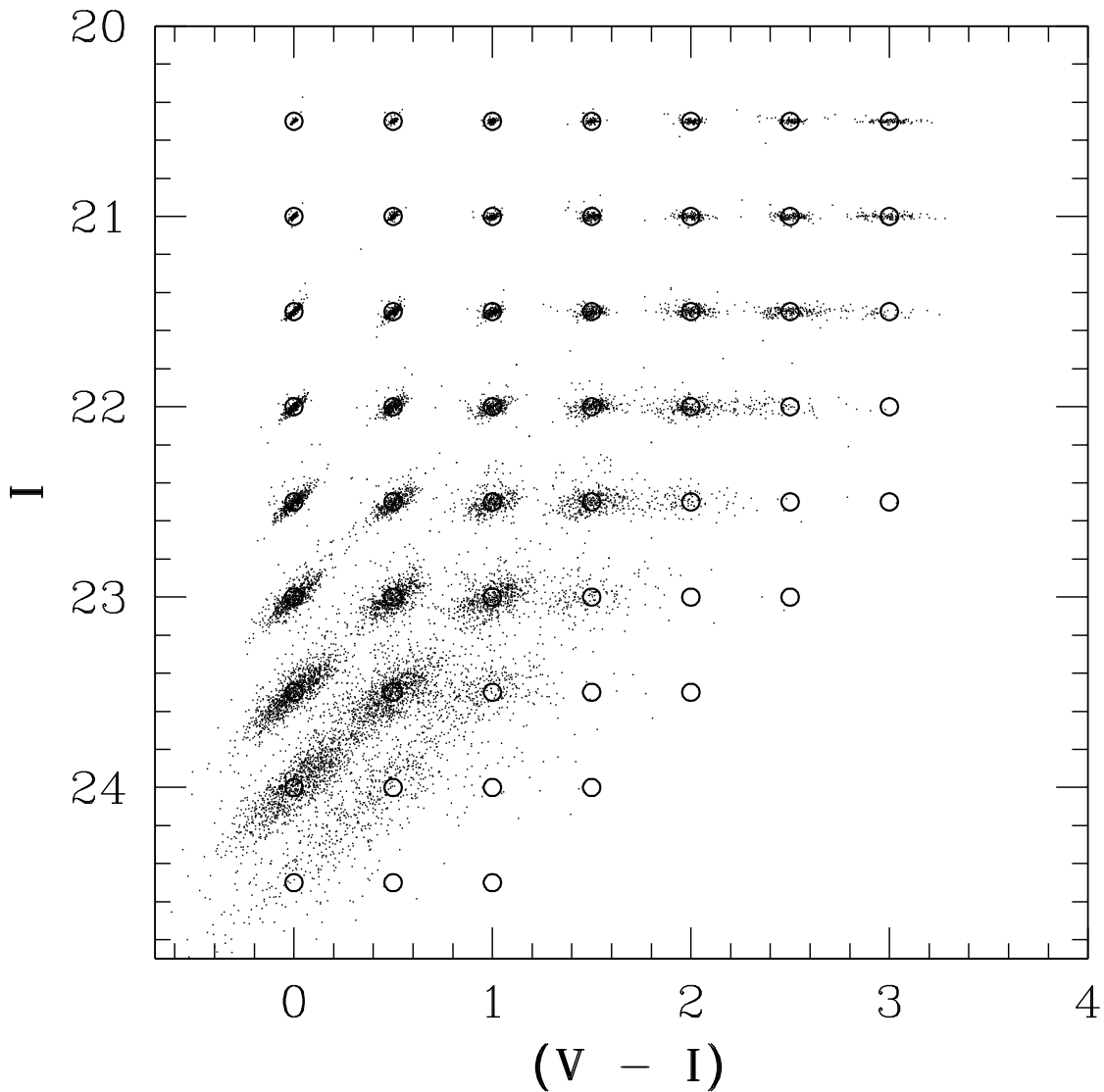


Fig. 4.— Color-magnitude diagram of artificial stars recovered from simulations on chip 1 on the $\mathcal{M}2$ field (for representation purposes – other chips are similar). The circles show the discrete I , $(V - I)$ locations for the added stars, and the points show the recovered values. Note the rather sharp transition in photometric completeness for stars with input $V \sim 24$

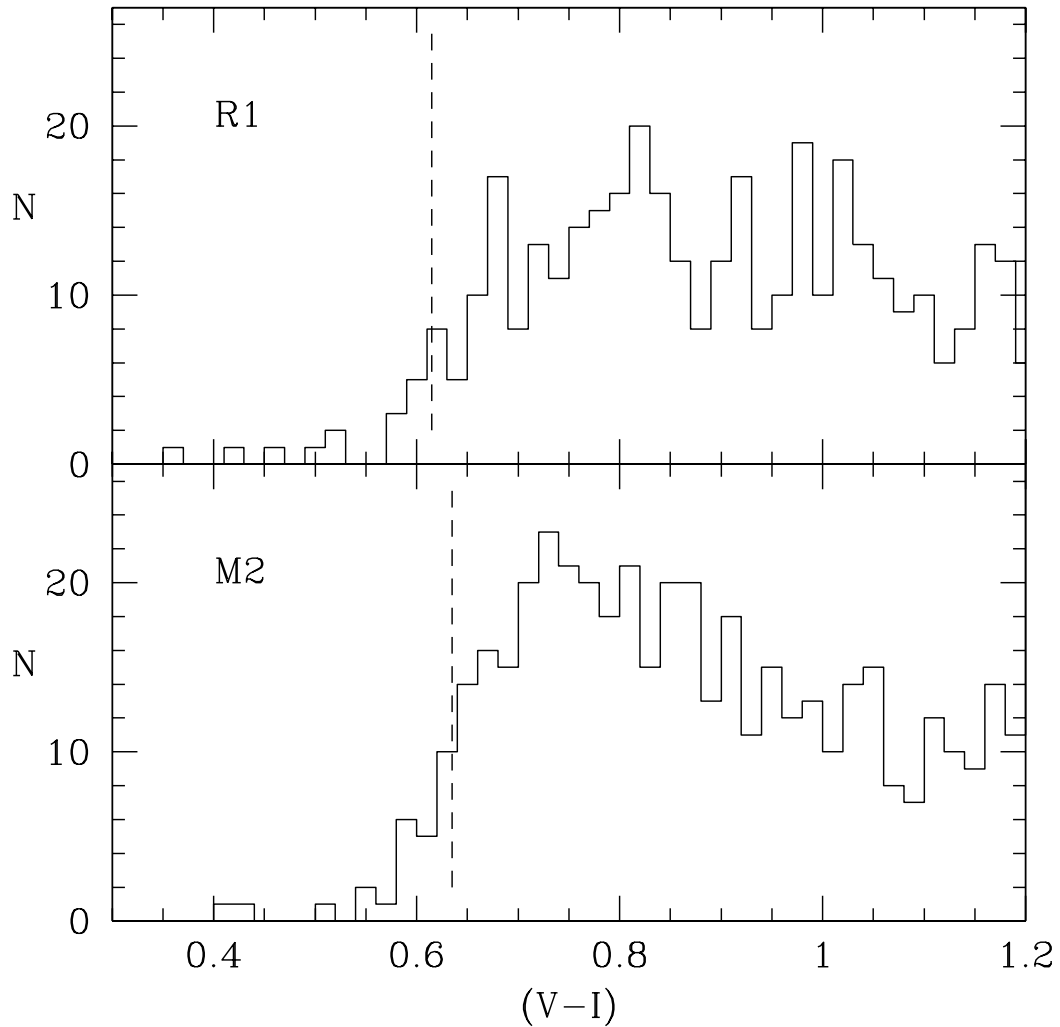


Fig. 5.— Color histograms for the bright stars ($17.0 < I < 20.5$) in the background $\mathcal{R}1$ field (top) and the $\mathcal{M}2$ field (bottom). In each case the dashed line shows the location of the blue edge of the color distribution as determined via an edge-detection filter (see text for details).

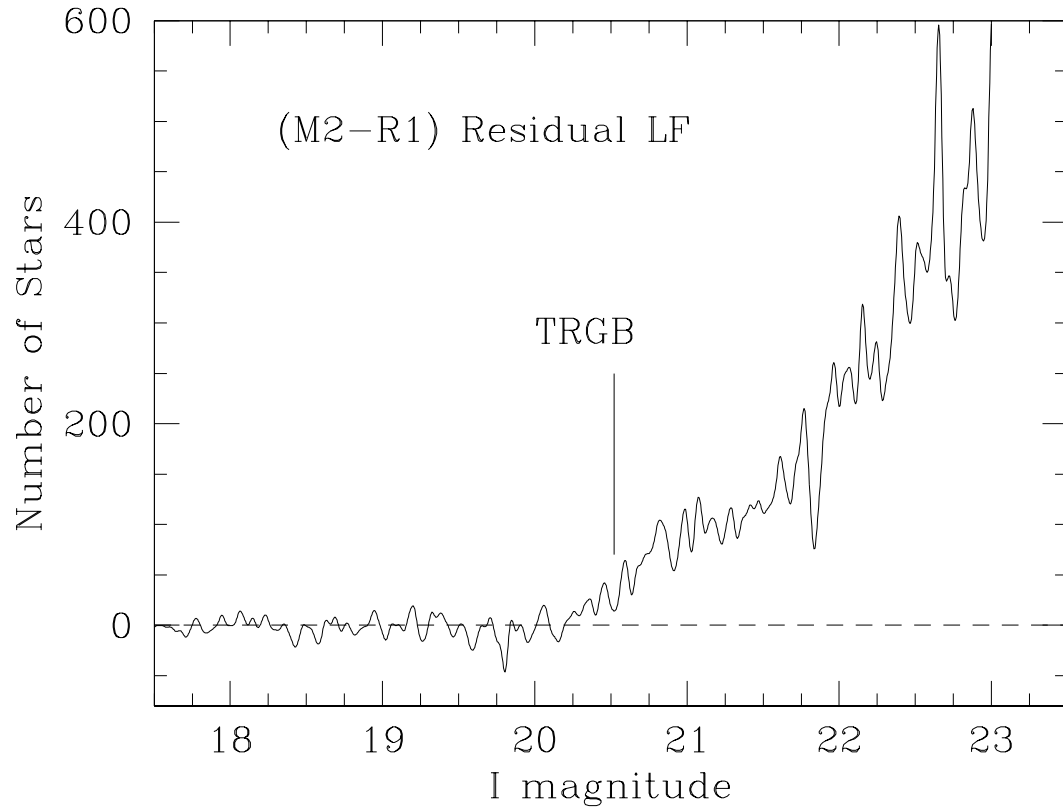


Fig. 6.— Smoothed residual I LF of the M31 halo field – the background LF. The solid line denotes the position of the tip of the RGB ($I_{TRGB} = 20.52 \pm 0.05$), derived using an edge-detection filter.

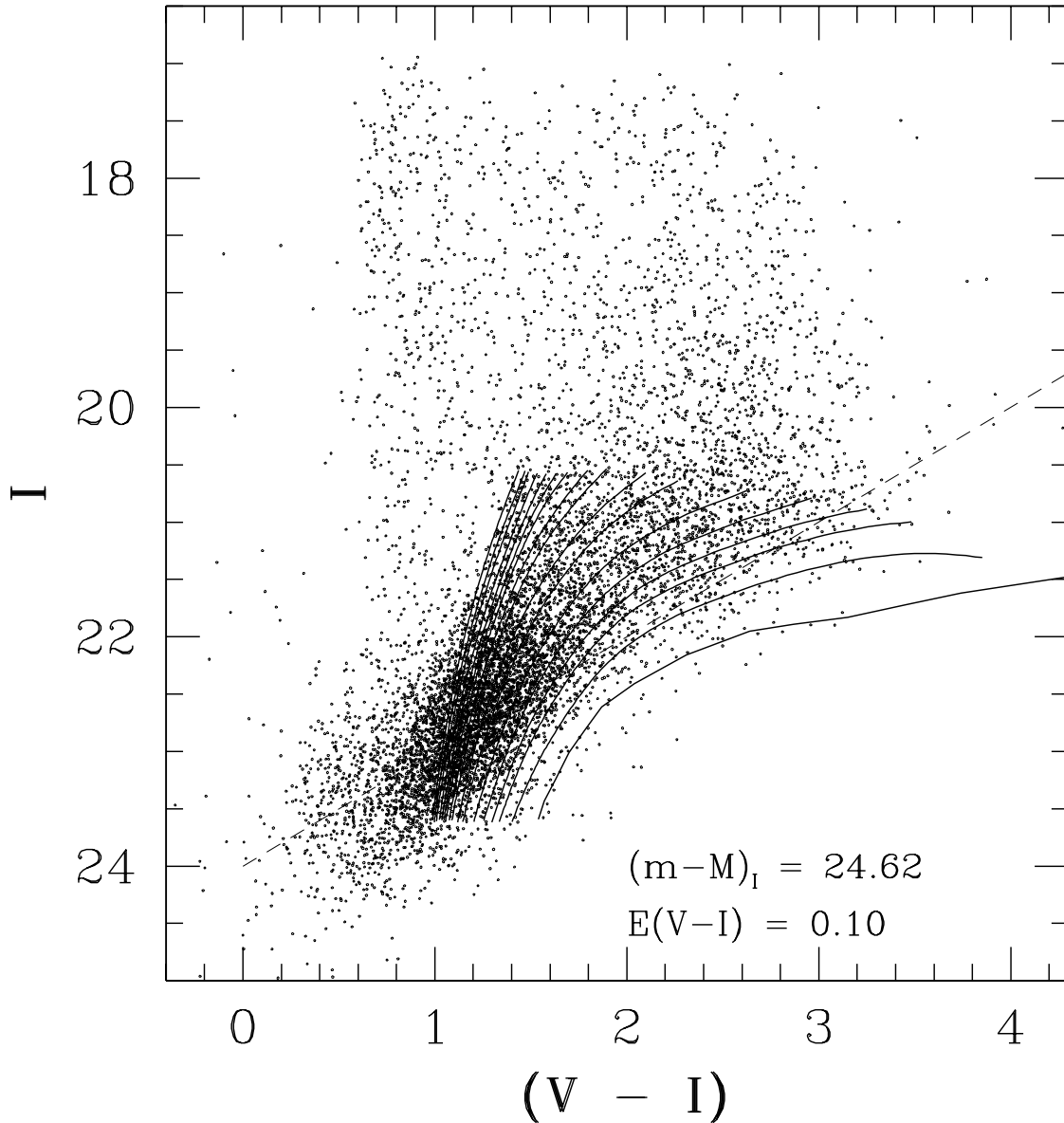


Fig. 7.— CMD for stars in the $M2$ field. The solid lines are evolutionary tracks for $0.8 M_{\odot}$ stars from VandenBerg et al. (2000), shifted to the given distance modulus and reddening. The models have been further shifted 0.03 mag to the blue (empirical correction - see text for more details). From left to right : $[Fe/H] = -2.31, -2.14, -2.01, -1.84, -1.71, -1.61, -1.54, -1.41, -1.31, -1.14, -1.01, -0.83, -0.71, -0.61, -0.53$ and -0.40 . The rightmost model is the $[Fe/H] = +0.07$ isochrone from Bertelli et al. (1994). The dashed line represents the 50% completeness level for the least-sensitive chip in the mosaic.

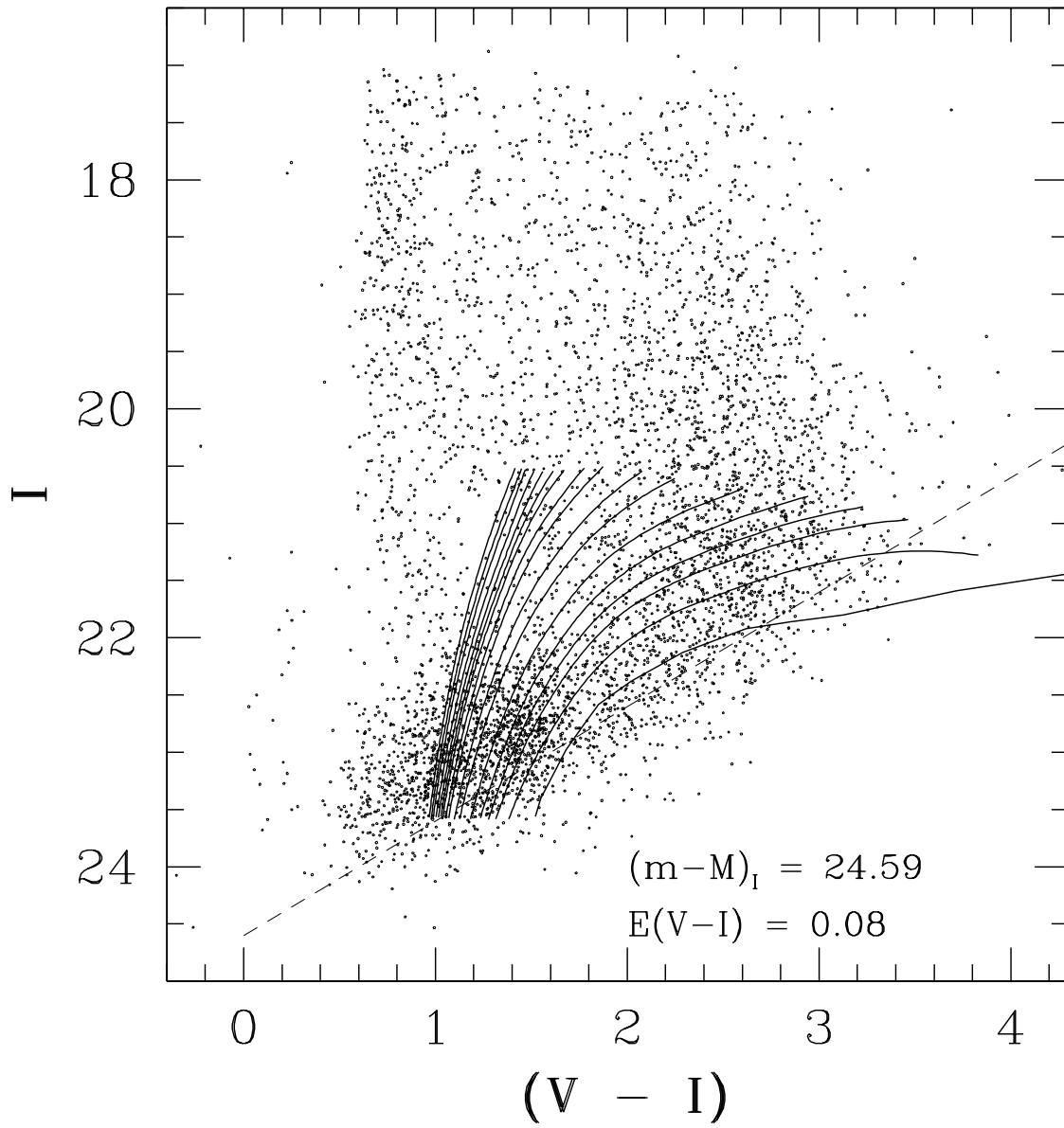


Fig. 8.— CMD for stars in the $\mathcal{R}1$ field. Solid lines are the same as in Figure 7. The dashed line represents the 50% completeness level for the least sensitive chip in the mosaic.

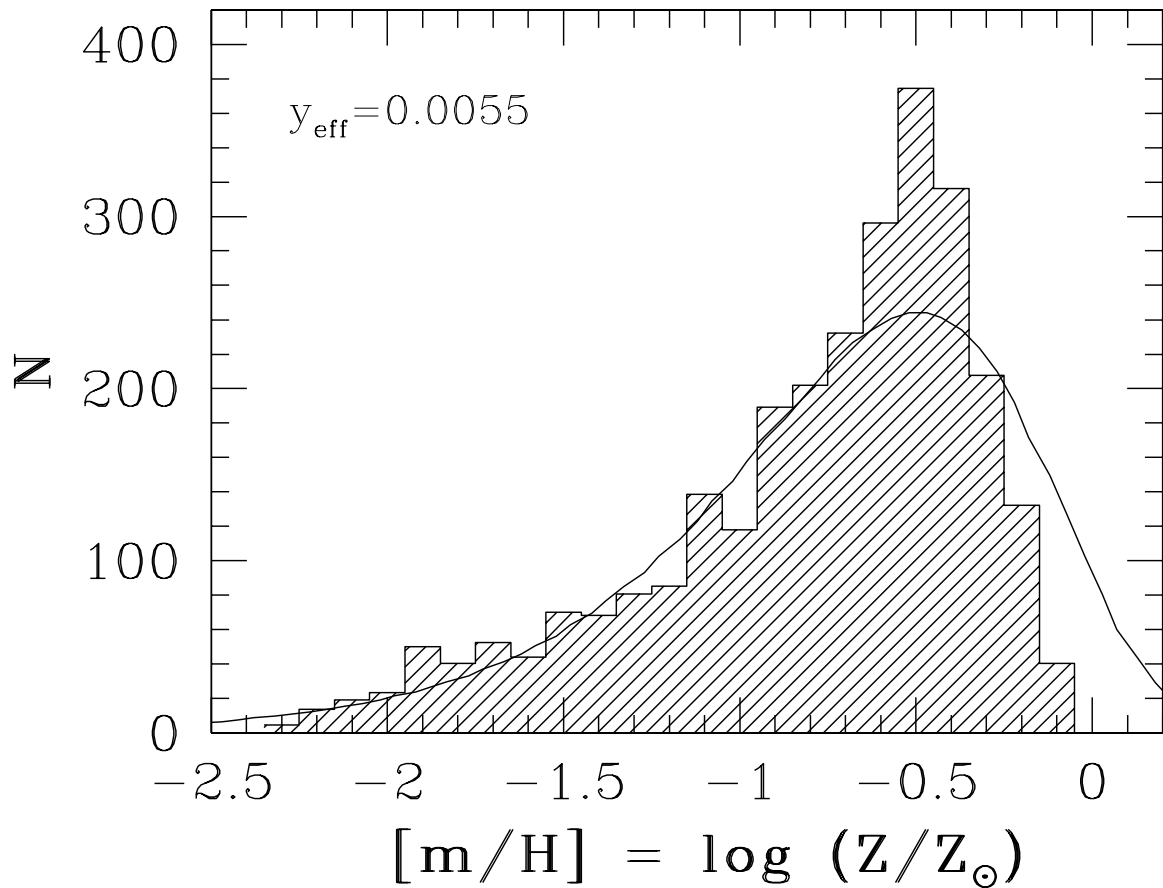


Fig. 9.— Metallicity Distribution Function (MDF) for all stars with $20.6 < I < 22.5$. The data has been corrected for both photometric completeness and for background contamination; see text for details. The solid line denotes a single-zone, closed-box chemical evolution model with a yield $y = 0.0055$.

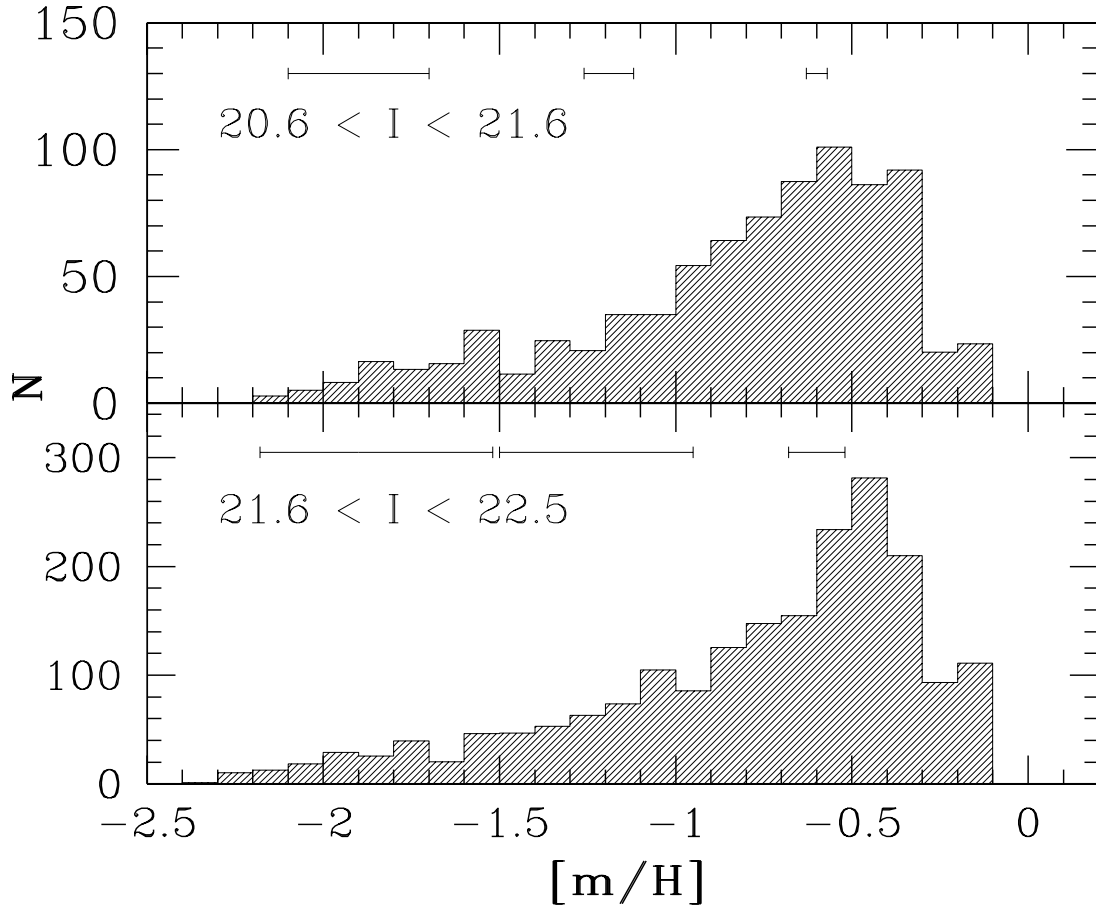


Fig. 10.— MDFs for M31 halo stars in the given magnitude ranges. The error bars represent the uncertainties in $[m/H]$ due to photometric errors at $I = 21$ (top) and $I = 22$ (bottom). As in Figure 9, all data has been background and incompleteness corrected.

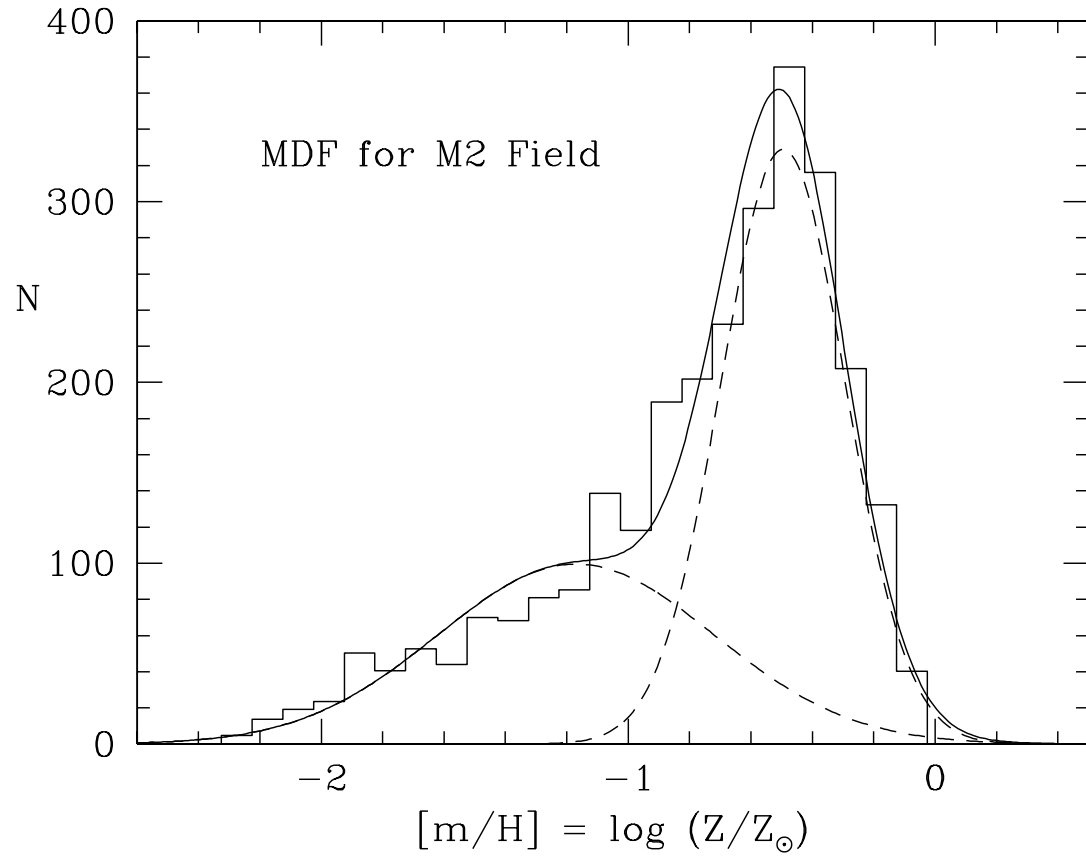


Fig. 11.— M31 MDF (for $20.6 < I < 22.5$) with best-fitting Gaussians (dashed lines) and the combination of both (solid line).

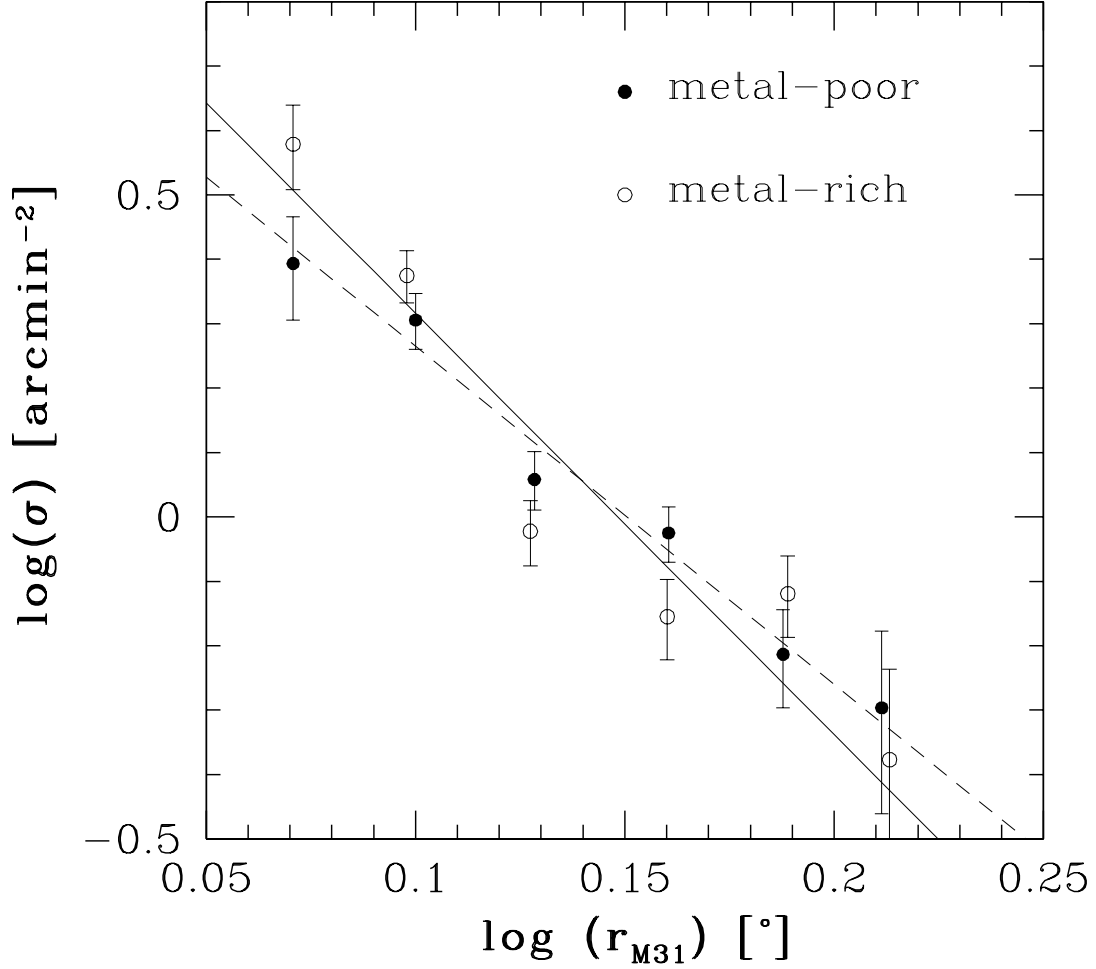


Fig. 12.— Log-log plot of the number density of stars in the MDF with $20.6 < I < 22.5$, as a function of radius from M31. Open circles denote those stars with $-2.5 < [m/H] < -1.0$ (metal-poor), the the filled circles are the metal-rich stars with $-0.6 < [m/H] < -0.3$. The metal-poor profile has been shifted upwards by a factor $\Delta \log(\sigma) = 0.12$ to match the total number of stars in the metal-rich profile. The solid line is the best least-squares fit to the metal-rich profile ($\gamma = -6.54 \pm 0.59$), while the dashed line represents the best fit to the metal-poor profile ($\gamma = -5.25 \pm 0.63$).

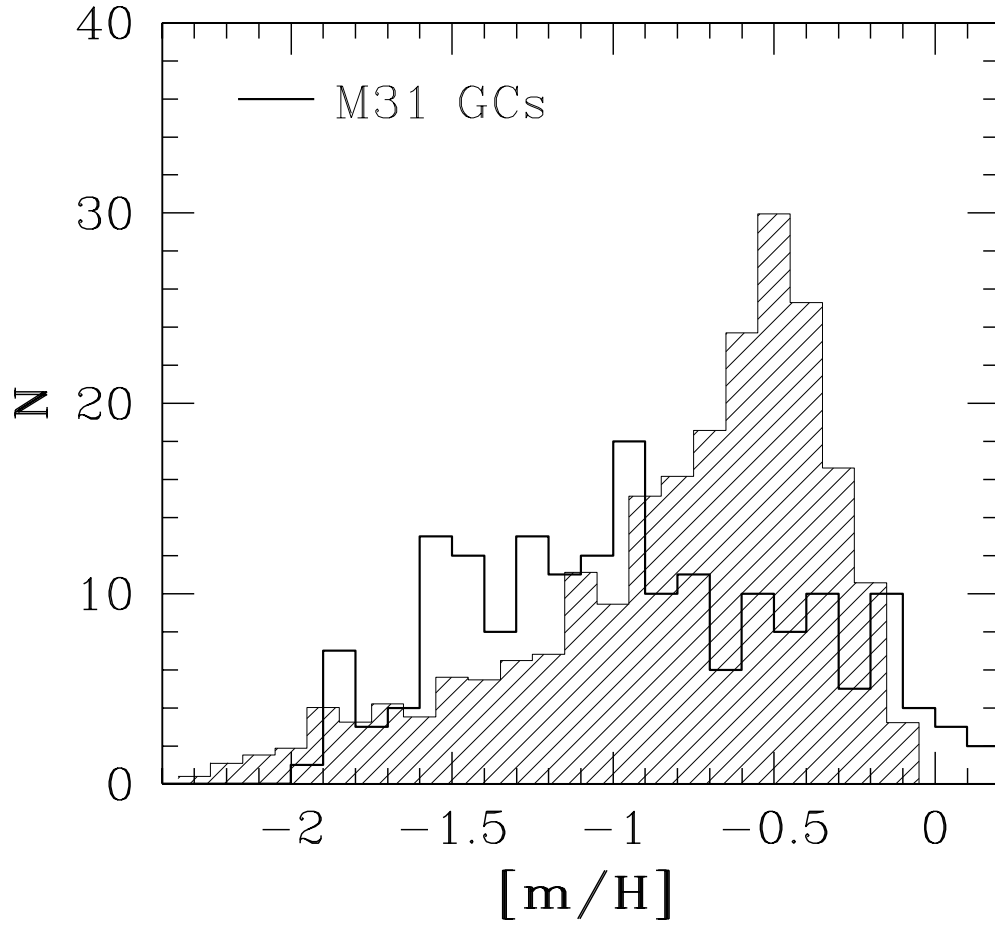


Fig. 13.— Comparison between the MDFs for the M31 halo field (hatched region) and the M31 globular clusters with spectroscopically-derived metallicities from Barmby et al.(2000). $[m/H] = [Fe/H] + 0.3$ has been applied to the GC metallicities.

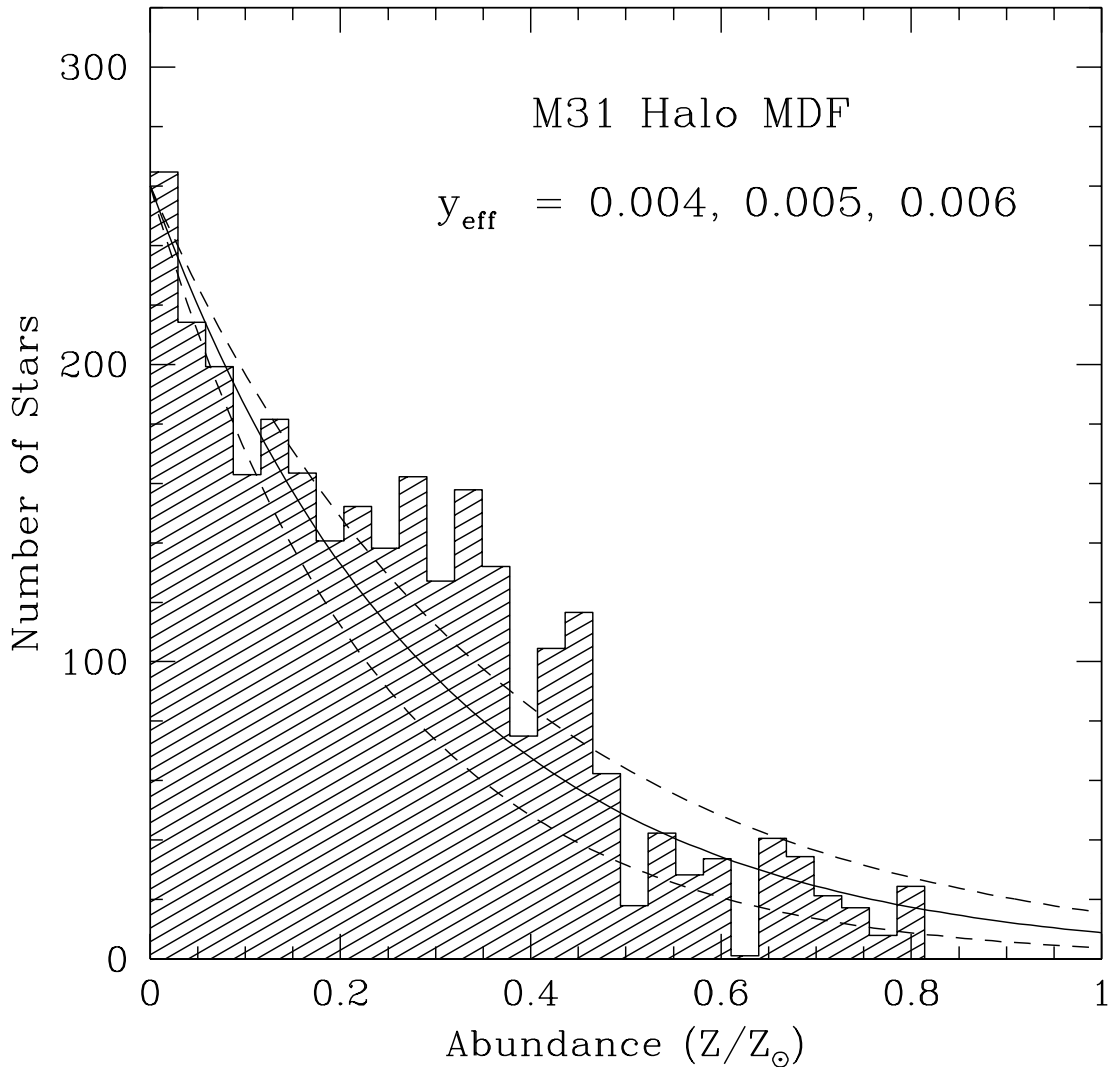


Fig. 14.— Linear metallicity distribution function of the number of stars as a function of metal-abundance Z . The three lines denote ‘leaky-box’ chemical evolution models with $y_{\text{eff}} = 0.004, 0.005, 0.006$, with $Z_o = 0$ and $Z_{\text{now}} = Z_{\odot}$. (The $y = 0.005$ model is the solid line, with the other two as dashed lines.)

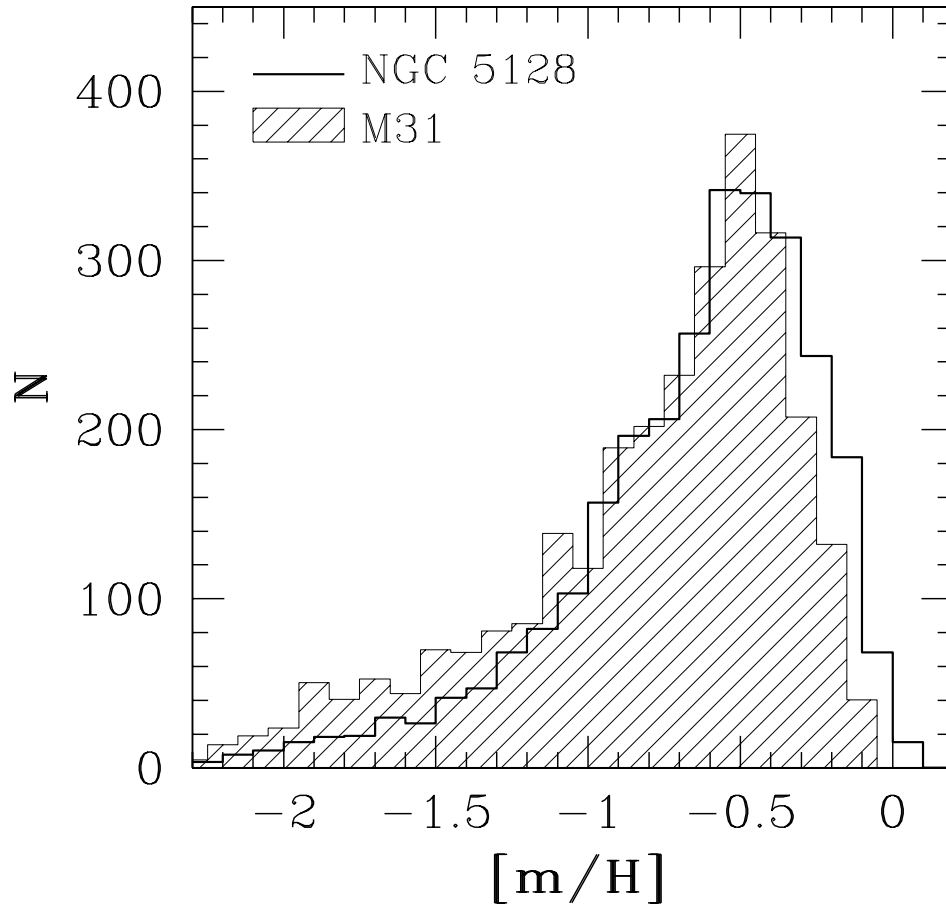


Fig. 15.— Comparison of the M31 halo MDF with the outer halo MDF for NGC 5128 (Harris et al. 1999; Harris & Harris 2000). The NGC 5128 data has been scaled by a factor 0.61 to normalize to the total number of total objects in both MDFs.